



Contents lists available at ScienceDirect

## Geoscience Frontiers

journal homepage: [www.elsevier.com/locate/gsf](http://www.elsevier.com/locate/gsf)

## Research Paper

## Bayesian geological and geophysical data fusion for the construction and uncertainty quantification of 3D geological models

Hugo K.H. Olierook<sup>a,e,\*</sup>, Richard Scalzo<sup>b</sup>, David Kohn<sup>c</sup>, Rohitash Chandra<sup>d,f</sup>, Ehsan Farahbakhsh<sup>b,d,f,g</sup>, Chris Clark<sup>a</sup>, Steven M. Reddy<sup>a</sup>, R. Dietmar Müller<sup>d</sup>

<sup>a</sup> School of Earth and Planetary Sciences, Curtin University, GPO Box U1987, Perth, WA, 6845, Australia

<sup>b</sup> Centre for Translational Data Science, University of Sydney, NSW, 2006, Sydney, Australia

<sup>c</sup> Sydney Informatics Hub, University of Sydney, NSW, 2006, Sydney, Australia

<sup>d</sup> EarthByte Group, School of Geosciences, University of Sydney, NSW, 2006, Sydney, Australia

<sup>e</sup> Timescales of Mineral Systems and John de Laeter Centre, Curtin University, GPO Box U1987, Perth, WA, 6845, Australia

<sup>f</sup> School of Mathematics and Statistics, University of New South Wales, Sydney, NSW, 2052, Australia

<sup>g</sup> Department of Mining Engineering, Amirkabir University of Technology (Tehran Polytechnic), Tehran, Iran

## ARTICLE INFO

## Keywords:

Capricorn orogen  
Machine learning  
Bayesian inference  
Markov chain Monte Carlo  
Solid earth  
Mineral exploration

## ABSTRACT

Traditional approaches to develop 3D geological models employ a mix of quantitative and qualitative scientific techniques, which do not fully provide quantification of uncertainty in the constructed models and fail to optimally weight geological field observations against constraints from geophysical data. Here, using the Bayesian Obsidian software package, we develop a methodology to fuse lithostratigraphic field observations with aeromagnetic and gravity data to build a 3D model in a small (13.5 km × 13.5 km) region of the Gascoyne Province, Western Australia. Our approach is validated by comparing 3D model results to independently-constrained geological maps and cross-sections produced by the Geological Survey of Western Australia. By fusing geological field data with aeromagnetic and gravity surveys, we show that 89% of the modelled region has >95% certainty for a particular geological unit for the given model and data. The boundaries between geological units are characterized by narrow regions with <95% certainty, which are typically 400–1000 m wide at the Earth's surface and 500–2000 m wide at depth. Beyond ~4 km depth, the model requires geophysical survey data with longer wavelengths (e.g., active seismic) to constrain the deeper subsurface. Although Obsidian was originally built for sedimentary basin problems, there is reasonable applicability to deformed terranes such as the Gascoyne Province. Ultimately, modification of the Bayesian engine to incorporate structural data will aid in developing more robust 3D models. Nevertheless, our results show that surface geological observations fused with geophysical survey data can yield reasonable 3D geological models with narrow uncertainty regions at the surface and shallow subsurface, which will be especially valuable for mineral exploration and the development of 3D geological models under cover.

## 1. Introduction

Surface mapping and subsurface interpretation of geological units are essential requirements for mineral exploration, and the wider geological and geophysical community. Geological units and their associated boundaries may share similar geological histories or may be juxtaposed to one another via unconformities or structural discontinuities such as faults or suture zones. Accurately positioning geological units and their

boundaries is fundamental for, but not limited to, constraining plate reconstructions (Cawood and Korsch, 2008; Merdith et al., 2017), defining stratigraphy (Gradstein et al., 2012), and successful mineral and petroleum exploration (Dentith and Mudge, 2014; Selley and Sonnenberg, 2014). In order to conceive a comprehensive model of both the surface and subsurface geology, a combination of geological mapping, geophysical interpretation, sample analysis and prior knowledge are used. Although all of these ingredients are important, traditional

\* Corresponding author. Timescales of Mineral Systems, Centre for Exploration Targeting – Curtin Node, School of Earth and Planetary Sciences, Curtin University, GPO Box U1987, Perth, WA, 6845, Australia.

E-mail address: [hugo.olierook@curtin.edu.au](mailto:hugo.olierook@curtin.edu.au) (H.K.H. Olierook).

Peer-review under responsibility of China University of Geosciences (Beijing).

<https://doi.org/10.1016/j.gsf.2020.04.015>

Received 15 August 2019; Received in revised form 11 February 2020; Accepted 25 April 2020

Available online xxxx

1674-9871/© 2020 China University of Geosciences (Beijing) and Peking University. Production and hosting by Elsevier B.V. This is an open access article under the CC BY-NC-ND license (<http://creativecommons.org/licenses/by-nc-nd/4.0/>).

workflows to incorporate them tend to produce only a handful of solutions that either neglect, or incompletely account for, the uncertainty associated with geological or geophysical interpretations, as well as the knowledge of how far to extrapolate data derived from sample analysis. This shortcoming of traditional geological model-building is exacerbated in regions with thick sedimentary or regolith ‘cover’ because the uncertainty poses a significant impediment to understanding the nature of the subsurface. In a future where exploration under cover has been recognized as vitally important for the mineral exploration sector (McFadden et al., 2012), developing geological models with accounted uncertainty is pivotal.

To develop robust geological models, it is important to quantify the uncertainty on the position and configuration of geological units. Previous work addressing the uncertainty problem included employing fuzzy logic and information entropy approaches to build semi-quantitative 3D geological models (Abedi and Norouzi, 2012; Joly et al., 2012; Wellmann and Regenauer-Lieb, 2012). However, these approaches still require a significant degree of human decision making into how to fuse disparate geoscientific datasets. Other approaches characterize uncertainty by generating ensembles of 3D models through perturbations of a set of underlying descriptive geometric parameters (Lindsay et al., 2013; Pakyuz-Charrier et al., 2018a, 2018b; de la Varga et al., 2019; Giraud et al., 2019). However, these approaches still largely elude the question of how the joint distribution of such parameters is meant to be derived. A fully quantitative and informative 3D geological model will fuse available constraints in a probabilistically rigorous fashion. Bayesian inference provides a suitable framework for doing this by using Markov chain Monte Carlo (MCMC) sampling methods for estimation and uncertainty quantification of free parameters. Previous studies using Bayesian inference in the geosciences have primarily focused on (i) geophysical joint inversions (Bosch et al., 2006; Shen et al., 2013; Giraud et al., 2017), (ii) fluid flow through permeable reservoirs for groundwater, hydrocarbon or carbon dioxide storage applications (Ye et al., 2010; Refsgaard et al., 2012; Seifert et al., 2012; Oladyshkin et al., 2013), (iii) geomorphologic and climate evolution (Hapke and Plant, 2010; Chandra et al., 2019; Pall et al., 2020), and (iv) fusion of structural geology data with geophysical datasets (Jessell et al., 2010, 2014; Grose et al., 2018; Pakyuz-Charrier et al., 2018b; Wellmann et al., 2018). Despite a clear need for Bayesian fusion of solid Earth geological and geophysical datasets (Jessell et al., 2010, 2014, 2018), there is still relatively little work in developing Bayesian-inferred 3D geological models, particularly detailed models at the local and camp-scale in a mineral exploration context. One particular research avenue, which we aim to address here, is whether geological field observations can be incorporated together with geophysical data in a Bayesian framework.

To attempt to incorporate geological field observations, we use the Obsidian software package (Reid et al., 2013; McCalman et al., 2014). Obsidian provides a platform for MCMC sampling of the posterior probability distribution for a parameterized model of the 3D structure and physical properties of geological formations. Here, the free parameters are estimated by MCMC with the sampling taking into account both the estimated prior probability of the existence of any particular formation, and the likelihood of that configuration producing all available geophysical survey data in the modelled region. Obsidian’s major strength is an efficient distributed implementation of an adaptive parallel-tempered MCMC algorithm (Miasojedow et al., 2013) capable of sampling from distributions that may have multiple local modes, such as those arising in inversion problems with limited prior information. Obsidian was originally designed for deep (~1–5 km) geothermal energy applications in sedimentary basins, which includes the ability to fuse airborne or surface geophysical surveys (e.g., aeromagnetics, gravity, magnetotellurics, temperature) with laterally-sparse geophysical drill hole data (e.g., geological unit depths, bore hole temperature, density) and drill hole geological units as prior points. Although previous iterations of the Obsidian software package could not fuse geological field observations made on the Earth’s surface with geophysical survey data,

relatively little amendment to the program is required to make this possible. The ability to incorporate surface geological data is vital for surface and near-surface applications (<1 km). Such applications include the mineral exploration sector but also extend to any igneous or metamorphic (‘hard-rock’) terranes. Unlike sparse drill hole data, surface geological observations provide high-resolution lateral constraints on 2D surface geological models that, together with geophysical survey data, permit the development of robust 3D geological models.

In this contribution, we extend the Obsidian software package to enable coupling of (i) airborne magnetic and gravity survey data (using petrophysical priors derived from surface samples) with (ii) geological field observations that inform the configuration of lithostratigraphic units at discrete points on the Earth’s surface. We demonstrate the validity of our techniques by building a model of a 13.5 km × 13.5 km subsection of the Gascoyne Province, Western Australia (Fig. 1), that is rich in data diversity and coverage. We explicitly avoid building a geological forward model (cf. Giraud et al., 2019) to replicate common situations in mineral exploration under cover where a ‘true’ geological model may be significantly in error. The output modelled results are compared to surface geological maps and interpreted cross-sections produced by the Geological Survey of Western Australia (GSWA; Fig. 2; Johnson et al., 2012). These maps were made primarily from geological mapping with input of geophysical data only utilized in regions of cover, such as is present in the southern part of the area (Fig. 2a). There are a few datasets available in the region that are not utilized in our model. (1) There are only a few ~10 m-deep drill holes in the southwestern corner of our modelled area, so drill hole data are omitted as these do not add further detail than surface observations provide. With a lack of drill hole data, our contribution is able to address the impact of solely surficial geological data on the model accuracy. The lack of prior information is

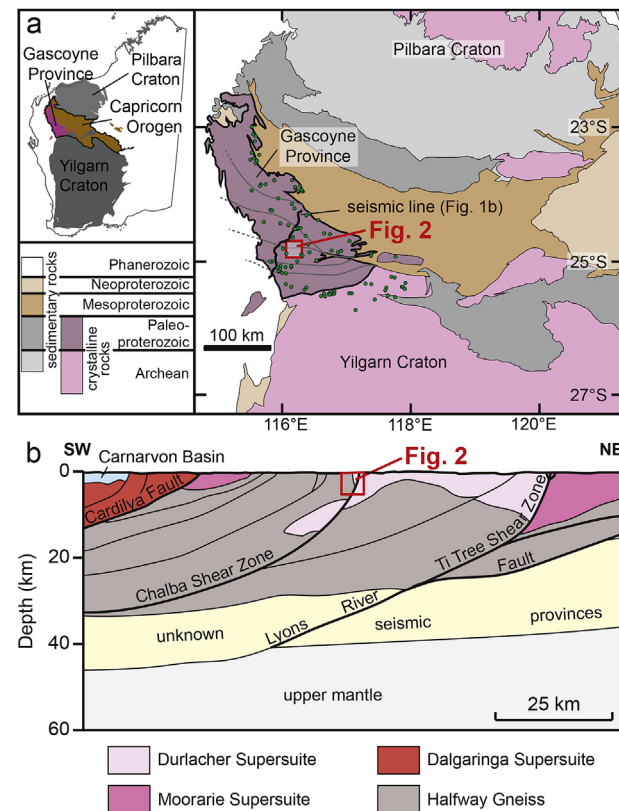


**Fig. 1.** (a) Geological map of the West Australian Craton, modified from Sheppard et al. (2016), showing location of seismic section and petrophysical data (green circles) from Aitken et al. (2014). (b) Interpretation of part of seismic line 10GA-CP2, after Johnson et al. (2013). The modelled region in this study is shown on both the map and seismic section (cf. Fig. 2).

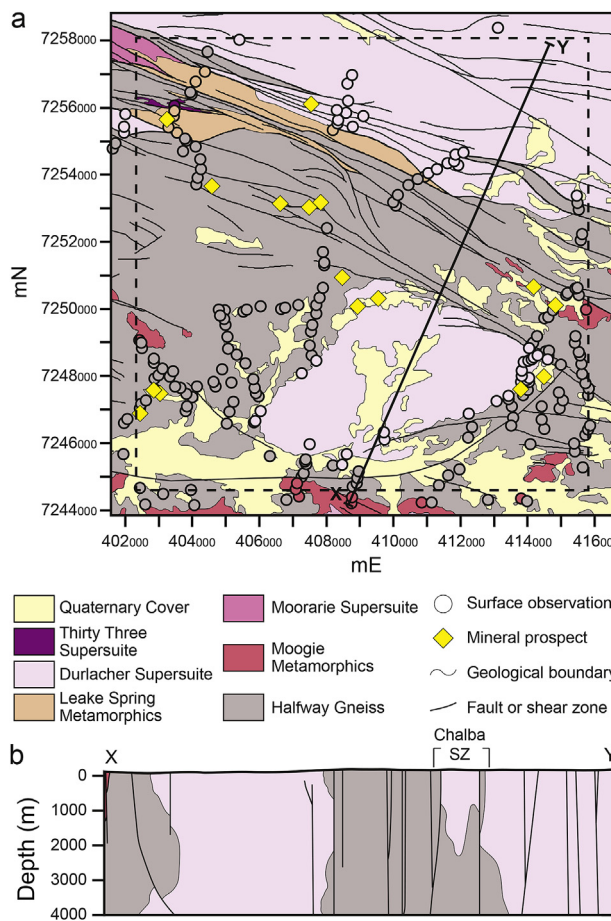


**Fig. 2.** (a) Detailed geological map of a 15 km × 15 km portion of the Gascoyne Province with the same centre as the modelled 13.5 km × 13.5 km area (dashed area), showing geological units, structural discontinuities (faults/shear zones), geological surface observations and mineral prospects and deposits. (b) Cross-section through detailed geological map, where vertical and horizontal scale are 1:1. Map and cross-section compiled using 1:100,000 geological maps from the Geological Survey of Western Australia.

particularly useful for applications that typically lack drill holes, such as greenfields mineral exploration or tectonic analysis of hard rock terranes. (2) Our study excludes the use of structural geological data because other workers have recently focussed on this problem (e.g., Pakyuz-Charrier et al., 2018b; Wellmann et al., 2018) and because Obsidian cannot yet incorporate structural data. Although this is clearly a drawback, future work will focus on attempting to incorporate structural geological data. (3) The single 2D active seismic line immediately to the west of our model (Fig. 1) is not utilized in a Bayesian framework because the vast majority of hard rock terranes do not have seismic data coverage. Despite these shortcomings, the model of the chosen study area is still particularly suitable for the future of mineral exploration as it exhibits a significant portion of recent sedimentary and regolith cover, which makes certain areas inaccessible for recording geological basement observations directly but possible to infer using Bayesian techniques applied to geophysical measurements.

## 2. Background

### 2.1. Geological setting of the Gascoyne Province

The Gascoyne Province, and the wider Capricorn Orogen, record the protracted amalgamation of the West Australian Craton and subsequent intracontinental tectonothermal activity (Figs. 1 and 2). Two main events

are thought to contribute to forming the West Australian Craton. First, the ca. 2195–2145 Ma Ophthalmia Orogeny sutured the Glenburgh Terrane, comprised of the Halfway Gneiss, to the Pilbara Craton (Rasmussen, 2005; Krapež et al., 2017). The deposition of the Moogie Metamorphics was associated with the Ophthalmia Orogeny, deposited into a foreland basin that formed in a response to the Glenburgh-Pilbara collision (Johnson et al., 2013). Second, the ca. 2005–1950 Ma Glenburgh Orogeny then amalgamated the combined Pilbara Craton-Glenburgh Terrane with the Yilgarn Craton to form the West Australian Craton (Johnson et al., 2013; Olierook et al., 2018). The Glenburgh Orogeny was associated with two major Andean-type granitoid formations, the Dalgaringa and Bertibubba Supersuites, and several subduction-related basins (Johnson et al., 2011; Olierook et al., 2018). After unification, the Capricorn Orogen experienced at least five intracontinental tectonomagmatic events, each decreasing in severity of tectonic character and magmatism (Johnson et al., 2017). The first two events, the 1830–1780 Ma Capricorn Orogeny and 1680–1620 Ma Mangaroon Orogeny, were both associated with significant granitoid magmatism of the Moorarie and Durlacher Supersuites, respectively (Sheppard et al., 2005, 2010a; Piechocka et al., 2017). Deposition of the Leake Springs Metamorphics was also concurrent with the early stages of the Capricorn Orogeny. Later events were predominantly amagmatic but were still associated with up to amphibolite-facies metamorphism and hydrothermal activity (Sheppard et al., 2007; Korhonen et al., 2017; Piechocka et al., 2018; Olierook et al., 2019a, 2019b; Agangi et al., 2020). Both suturing and intracontinental tectonic events have developed a pervasive east–west striking structural fabric in the Gascoyne Province that has compartmentalized the region into several geological zones that share tectonic characteristics (Sheppard et al., 2010a). In the south, zone and formation boundaries trend NE–SW whereas major structures are oriented NW–SE in the north, yielding a wedge-shaped geometry for the Gascoyne Province (Figs. 1 and 2). Compared to the rest of the Capricorn Orogen, the Gascoyne Province is relatively well exposed but there are still significant areas covered by recent regolith and sediment that hamper mineral exploration.

### 2.2. Bayesian inversion and inference

Inverse problems aim to recover the causal factors that produced a set of observations (Mosegaard and Tarantola, 1995; Sambridge and Mosegaard, 2002). For geological and geophysical applications, the objective of inverse problems is to recover the subsurface properties such as density and magnetic susceptibility from surface-based geophysical survey measurements of gravitational acceleration and magnetic field strength. However, geophysical surveys cannot yield unique solutions of the subsurface petrophysical properties. Thus, there are an infinite number of subsurface petrophysical measurement configurations that would produce the same survey readings (Sambridge, 1999; Sambridge and Mosegaard, 2002). Given that there is no unique solution, there is no reason to prefer one model over another without introducing constraints on what form the model should take (Parker, 1977; Sambridge and Mosegaard, 2002). Ways to introduce such constraints include 3D geometry inversion (Fullagar et al., 2008; Guillen et al., 2008), level-set inversions (Bijani et al., 2017; Zheglova et al., 2018) and (cross-) gradient regularization (Scholl et al., 2016; Giraud et al., 2019). However, these techniques are deterministic, yielding a single geological-geophysical inverse model that represents only one scenario (Bijani et al., 2017; Zheglova et al., 2018).

An alternative approach is to use sampling over all possible models in a probabilistic Bayesian context, which provides a more systematic approach towards uncertainty quantification and the incorporation of prior constraints. The Bayesian paradigm departs from traditional deterministic inversions in two main respects. First, it encapsulates prior knowledge about the geological model (before the data are taken into account) in terms of a probability distribution  $P(\theta)$  over model parameters  $\theta$ , called the prior. The probability  $P(D|\theta)$  of the data  $D$  conditioned

on a set of model parameters, called the likelihood, takes the place of the usual misfit function in a traditional inversion. Given these two elements, the posterior distribution  $P(\theta|D)$  of the model parameters given the data is given by Bayes' rule:

$$P(\theta|D) \propto P(D|\theta) P(\theta) \quad (1)$$

Second, in Bayesian reasoning the full posterior distribution is the quantity of interest, rather than a point estimate (as in maximum likelihood or maximum a posteriori) or, in some cases, a point estimate with a parameter covariance matrix describing the shape of a single posterior mode.

MCMC methods represent the posterior distribution by drawing a finite number of representative samples of parameter sets. Although computationally expensive (Tarantola and Valette, 1982; Sen and Stoffa, 1996), they have the advantages of not needing to calculate the unknown constant of proportionality in Eq. (1), and of representing the exact posterior in the limit of large numbers of samples, rather than some parametric approximation to the posterior. To do this, samples (proposals) are drawn from a target distribution by constructing a Markov chain for which the desired posterior is the invariant distribution (Hastings, 1970; Kass et al., 1998; Metropolis et al., 1953; Raftery and Lewis, 1996; van Ravenzwaaij et al., 2018). Convergence criteria determine when to stop sampling that, for example, could be a predetermined number of samples or an assessment of the behaviour of the likelihood function. However, for complex and large-scale 3D inversion problems, convergence can be challenging due to the large number of free parameters that need to be sampled effectively in limited computation time (i.e., high dimensionality; Sen and Stoffa, 1996).

For multimodal posteriors, the Markov chain can become trapped in a single mode and cannot fully explore the posterior distribution, making sampling much less efficient or causing the chain to converge to the wrong distribution. Parallel tempering (PT) is a sophisticated MCMC method (PT-MCMC, Fig. 3) that aims to increase the efficiency of the exploration of multimodal posterior distributions (Geyer, 1993; Fukushima and Nemoto, 1996; Sambridge, 2013). Parallel tempering uses a number of replicas of the original sampling method, where the

replicas are created at different 'temperatures' (Earl and Deem, 2005; Brooks et al., 2011) by rescaling the likelihood probability density function (Sambridge, 2013). High temperature replicas sample a smoother (flatter) version of the likelihood function in order to 'escape' from local minima and provide global exploration features (Fig. 3). Conversely, low temperature replicas provide local exploration capabilities. Hence, with parallel tempering, there is a delicate balance between global and local exploration (Earl and Deem, 2005; Sambridge, 2013). During sampling, the replicas are able to exchange their configurations, typically between neighbouring replicas via the Metropolis–Hastings proposal (Sambridge, 2013). Ultimately, this improves the mixing of Markov chain (i.e., thorough exploration of space and convergence to the target distribution) and efficiency of convergence (Sambridge, 2013).

### 2.3. Obsidian software package for joint geophysical inversion

The Obsidian software package was originally designed for geothermal exploration in sedimentary basins. Here, we provide a brief overview of the salient features that are important for our inverse problem. For a detailed background of Obsidian, the reader is referred to Ramos et al. (2012), Reid et al. (2013), McCalman et al. (2014), Beardmore et al. (2016) and Scalzo et al. (2019). For completeness, we briefly describe the critical elements of the inversion framework here.

Obsidian's 3D model consists of  $N$  layers with petrophysical properties (in this case, mass density  $\rho_i$  and magnetic susceptibility  $\chi_{M,i}$ ) that are spatially constant within each layer. The depth to the top of layer  $i$  at the  $j^{\text{th}}$  control point  $(x_j, y_j)$  on a regularly spaced rectangular grid across the modelled area is labeled  $\zeta_{ij}$ . Let  $\theta$  denote the totality of these parameters.

In each iteration of the Obsidian workflow, the petrophysical properties for this parameterized 3D model are discretized onto a grid of voxels. Each layer depth  $z_i(x, y)$  across the modelled area is interpolated from the  $\zeta_{ij}$ , using a two-dimensional Gaussian process regression with a square exponential covariance kernel, where the covariance length in each direction matches the lateral spacing between control points. The constraint  $z_i(x, y) \leq z_{i+1}(x, y)$  for each layer  $i$  is enforced on the discretized grid, setting the thickness of layer  $i$  at location  $(x, y)$  to  $D_z(x, y) = \max(0, z_{i+1}(x, y) - z_i(x, y))$ . This allows layers with no coverage in a particular region to "pinch out" to zero thickness; each layer interface is differentiable, except possibly at the lateral boundary of a pinched-out region. The rock properties beyond the horizontal boundaries are padded with constant values continuous with the properties evaluated on the boundary. The expected geophysical sensor readings are then forward-modelled, using rectangular prism approximations for the gravitational field (Li and Oldenburg, 1998) and total magnetic anomaly (Li and Oldenburg, 1996, 1998). Lithostratigraphic observations are forward-modelled by sampling the discretized model at the surface. Obsidian is also capable of forward-modelling other sensors, including 1D magnetotellurics, temperature, and reflection seismology, although seismic measurements may be more efficiently incorporated as priors on the depth to each layer.

The model prior and likelihood are then calculated using the given parameter values and the forward-modelled data. The prior distribution  $P(\rho_i, \chi_{M,i})$  for mass density and magnetic susceptibility is multivariate Gaussian, informed by petrophysical measurements from the literature. The priors  $P(\zeta_{ij})$  on the control points for the depth to layer  $i$  are also Gaussian, with user-defined mean and variance if drill cores and/or seismic interpretation are available. The likelihood models for the various datasets are described in more detail in section 3.4 below.

## 3. Materials and methods

### 3.1. 3D geological model parameterization

The construction of the parameterized 3D geological model in the chosen 13.5 km × 13.5 km area in the Gascoyne Province involves four types of data: (i) a hierarchical construction of layers using available 2D

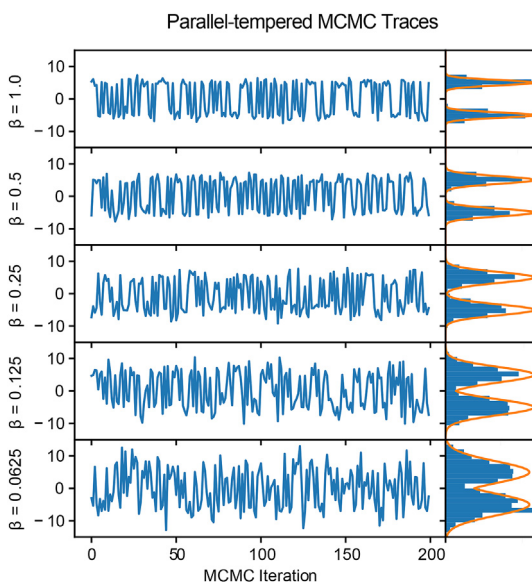


**Fig. 3.** Illustration of how parallel-tempered Markov chain Monte Carlo explores multi-modal distributions. Trace plots are shown for sampling of a mixture of two well-separated Gaussian distributions, with each trace corresponding to a different value of the inverse temperature parameter  $\beta$ . In the chain with the lowest value of  $\beta$ , the modes are explored freely; proposals that swap states between adjacent chains on the  $\beta$  ladder enable exchange of information to the  $\beta = 1$  chain, allowing it to explore both Gaussian modes readily.

seismic data interpretation (Fig. 1b; Johnson et al., 2013), (ii) two types of point-based measurements — magnetic and density data — on hand samples from Aitken et al. (2014), (iii) regional aeromagnetic and gravity data (Geological Survey of Western Australia, 1996; Mathews and Jecks, 2010), and (iv) geological field observations from the Western Australian Rocks (WAROX) database. A two-dimensional seismic survey was conducted in 2011 (Johnson et al., 2013). The surface position of the seismic line is immediately to the west of our study area and, thus, probably cross-cuts the same geological units that are present in our area (Fig. 1a). The seismic interpretation of Johnson et al. (2013), aided by geochronological data, directly informs that the stratigraphic units in the 3D geological model, from oldest to youngest, are the: (i) ca. 2550–2430 Ma Halfway Gneiss (Johnson et al., 2017), (ii) ca. 2210–2150 Ma Moogie Metamorphics (Martin and Morris, 2010), (iii) ca. 1840–1810 Ma Leake Spring Metamorphics and ca. 1830–1780 Ma Moorarie Supersuite (Sheppard et al., 2010b; Johnson et al., 2011), (iv) ca. 1690–1660 Ma Durlacher Supersuite (Sheppard et al., 2005; Piechocka et al., 2017), and (v) ca. 995–900 Ma Thirty Three Supersuite (Sheppard et al., 2010b; Piechocka et al., 2017). In the chosen 13.5 km × 13.5 km area, only the Halfway Gneiss and Durlacher Supersuite are areally significant, comprising ~59% and ~35% of the interpreted area by GSWA (Fig. 2). Other areally-minor units in the 13.5 km × 13.5 km area include the Leake Spring Metamorphics (~3%), Moogie Metamorphics (~2%), Moorarie Supersuite (<1%) and Thirty Three Supersuite (<1%). Only the two volumetrically-major units are modelled in this study as the other units appear primarily near the surface (Johnson et al., 2011), and are also present only in areas smaller than our model can resolve (see next paragraph). Resolving finer-scale features is out of the scope of this contribution.

The square area is tiled with a 5 × 5 grid of control points defining the boundary between the Halfway Gneiss and Durlacher Supersuite. Including mass density and magnetic susceptibility defined for both rock layers, the model has 29 parameters in total. A Gaussian prior with mean zero and standard deviation of 5 km is placed over the depth to the interface, reflecting only vague prior knowledge about the location of the boundary, and allowing either formation to be accessible at the surface. This parameterized model is discretized with resolution of 500 m during the forward model calculations for the potential fields through the prism approximation; the parametrization can be directly queried at the surface for lithostratigraphic measurements so that no spatial discretization is needed.

### 3.2. Petrophysical data

Two types of petrophysical data, magnetic susceptibility and density, were collected on hand samples (Aitken et al., 2014) to link to aeromagnetic and gravity data, respectively (Fig. 4). A relatively low number

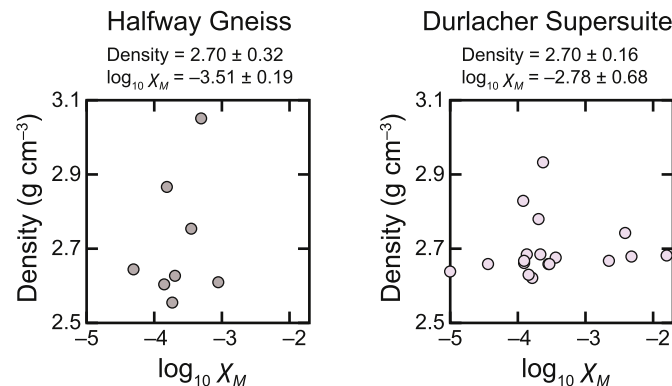


**Fig. 4.** Measured density and magnetic susceptibility ( $\log_{10} \chi_M$ ) for modelled geological units: (a) Halfway Gneiss, (b) Durlacher Supersuite. Mean density and susceptibility errors are quoted at  $2\sigma$  uncertainty.

of magnetic ( $n = 104$ ) and density ( $n = 103$ ) samples across the entire Gascoyne Province were available (Aitken et al., 2014). Thus, the sample mean and covariance of magnetic and density measurements for each geological unit were used to inform a multivariate Gaussian prior, acknowledging that spatial differences in magnetic and density distributions cannot be captured in this contribution.

### 3.3. Geophysical and geological data

Two geophysical survey data are employed, namely aeromagnetic

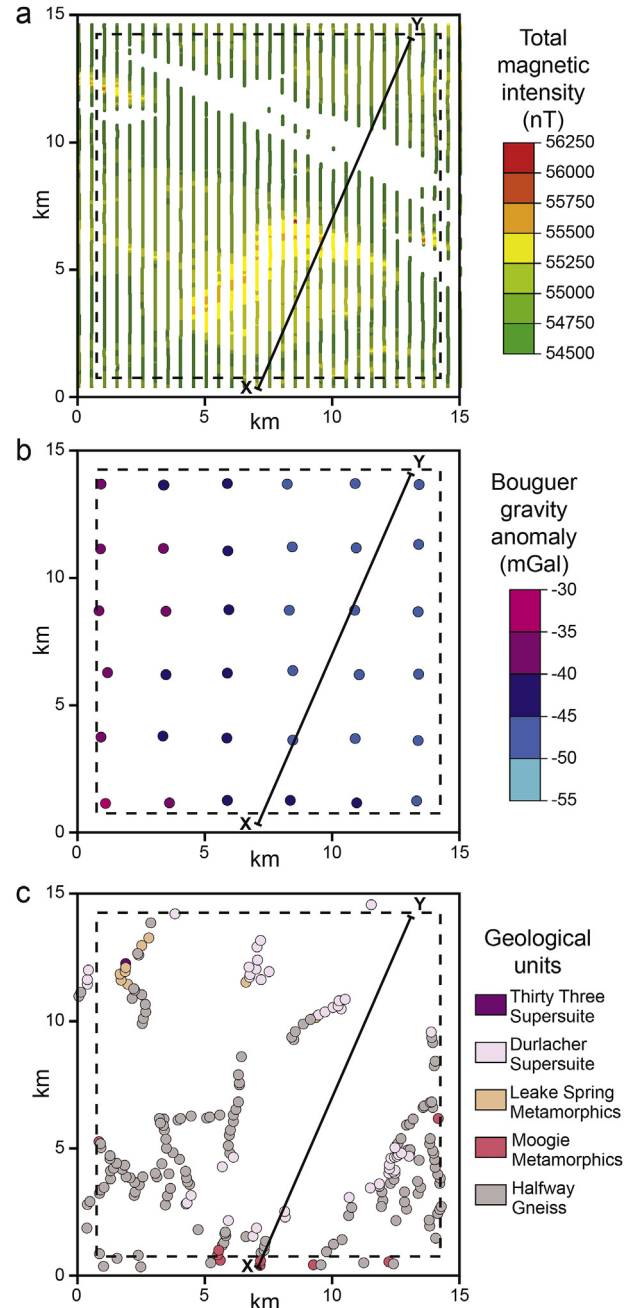


**Fig. 5.** Measured geophysical survey data and geological field observations for 15 km × 15 km area, with dashed line representing modelled 13.5 km × 13.5 km area. (a) Aeromagnetic data, showing locations of measured data on flight lines. (b) Gravity data, showing locations of ground-based measuring stations. (c) Geological field observations. Note the paucity of units other than the Halfway Gneiss and Durlacher Supersuite. X-Y line corresponds to cross-section line in Fig. 2.

(Fig. 5a) and gravity data (Fig. 5b), that are forward-modelled to correspond to sample-based magnetic susceptibility and density data, respectively. These types of geophysical surveys were already available for incorporation in the Obsidian framework. In addition to the geophysical data, field-based geological units observations are incorporated into Obsidian (Fig. 5c).

Aeromagnetic data in the study area (Fig. 5a) utilized a subsection of the 1995/96 Bangemall Survey directed by GSWA from latitudes 23.5°–26.0° S and longitudes 115.0°–120.0° E (Geological Survey of Western Australia, 1996). The Bangemall aeromagnetic data were flown at a 7.5 m sample interval, 500 m flight line spacing and a mean terrain clearance of 60 m. The final magnetic intensity in nT has the following corrections from the raw data: (i) the 1990 IGRF model removed and a base value of 54940 nT added, (ii) diurnal correction applied, with a base value of 55220 nT, (iii) parallax correction of 0.4 fiducial applied, (iv) levelled using tie line information, and (v) tie lines force levelled to flight lines. The original horizontal datum of the Bangemall Survey was the AGD84, projected using AMG zone 50, but this was converted to the WGS84, zone 50S for each data point. The flight path vector data were explicitly favoured over the post-processed raster data to avoid introducing correlations. Very finely, regularly-sampled raster data are often preferred in order to apply fast Fourier transform inversion techniques. However, resampling or interpolating non-gridded data onto such a grid results in correlations between the gridded data points, which can lead to biases and incorrect results in probabilistic inversions if not explicitly accounted for (Scalzo et al., 2019).

Gravity anomaly data in the study area (Fig. 5b) were derived from the 2010 Gascoyne North and Gascoyne South surveys directed by GSWA from latitudes 23.5°–26.0° S and longitudes 115.2°–118.5° E (Mathews and Jecks, 2010). The Gascoyne North and South gravity data were acquired at a ground-based nominal station spacing of 2500 m in a square grid configuration. The final complete spherical cap Bouguer anomaly in  $\mu\text{ms}^{-2}$  had the following corrections from the raw data: (i) correction of remanent drift, typically less than  $0.05 \mu\text{ms}^{-2} \text{ h}^{-1}$ , (ii) computation of Bouguer anomaly using a modified spreadsheet developed by M. Bacchin of Geoscience Australia, (iii) spherical cap Bouguer anomaly computation relative to the Australian Absolute Gravity Datum 2007, and (iv) terrain correction using the AUSGEOD09 vertical coordinate reference frame. The original horizontal datum was GDA94, which is equivalent to WGS84. Similar to the magnetic data, the located surface point-based data were explicitly favoured over the post-processed raster data.

Lithostratigraphic unit observations made at the surface were obtained from the Western Australian Rocks (WAROX) database, available from GSWA (Figs. 2 and 5c). Each spatially-referenced sample point records an observation of rock type coupled to an interpreted geological unit. Designation of a particular geological unit is informed from petrographic, geochemical and geochronological knowledge obtained on a subset of WAROX data. For example, the assignment of a geological unit is near certain where U-Pb crystallization ages are available or where whole-rock major and trace element geochemistry has been collected. In the chosen  $13.5 \text{ km} \times 13.5 \text{ km}$  study area, only one sample has geochronological and geochemical information (Fig. 5c). However, there are more than 100 age and over 500 samples with geochronological and geochemical data, respectively, in the Gascoyne Province from the same geological units that are present in the  $13.5 \text{ km} \times 13.5 \text{ km}$  study area (e.g., Johnson et al., 2017). All samples with U-Pb ages and/or geochemical data in the Gascoyne Province also have petrographic and/or hand sample descriptions, which can be used to inform the geological unit for geological surface observations where only hand sample or petrographic descriptions are available. Even though inference of geological units from similar petrographic and hand sample descriptions is relatively robust, it may be in error. Thus, we have accounted for this potential uncertainty in geological field observations (see section 3.4 for further details). All our observations were taken at the surface but could be readily used where geological unit observations could be made in the subsurface (i.e., via drill hole information). The formation that is

observed at the surface defines the value of a given field observation.

### 3.4. Likelihood models

Given the forward-modelled predictions  $f_s(g(\theta))$  for the observations  $D_s$  of a geophysical sensor s based on a discretized 3-D model  $g(\theta)$ , the likelihood is:

$$P(D_s | \theta) = t_{2as} \left( [f_s(g(\theta)) - D_s] \times \sqrt{\frac{\alpha_s}{\beta_s}} \right) \quad (2)$$

where  $t_v(x)$  denotes the Student's-t distribution with  $v$  degrees of freedom (McCalman et al., 2014; Scalzo et al., 2019). The t distribution has fairly thick tails compared to the Gaussian distribution. It arises in this case by assuming that each sensor has Gaussian noise with unknown variance, and by averaging the underlying Gaussian likelihood over all possible values of this noise variance for each sensor (see Appendix A). The hyperparameters  $\alpha_s$  and  $\beta_s$  describe the shape of an inverse-gamma distribution  $\text{IG}(x; \alpha_s, \beta_s)$  that forms the prior on the noise variance for each sensor;  $\beta_s$  provides an overall variance scale, while  $\alpha_s$  controls the tails of the distribution, with smaller  $\alpha_s$  corresponding to a heavier tail towards large possible variance. Integrating out the noise variance in this way helps to speed up sampling. We choose  $\alpha_s = 1, \beta_s = 0.2$  for each sensor, producing a 95% credible interval for the noise variance of  $0.05 < \sigma^2 < 3$  (as a fraction of the sample variance of the data) with 95% credibility.

In a similar manner, we formulate a likelihood for categorically-distributed lithostratigraphic observations. Supposing that these observations have some unknown probability  $p$  of being correct (that is, that the true underlying rock formation corresponds to the geologist's interpretation) in the absence of corroborating geochronological or geochemical information, we consider an underlying binomial likelihood,

$$P(k|n, p) = \frac{\Gamma(n+1)}{\Gamma(k+1)\Gamma(n-k+1)} p^k (1-p)^{n-k} \quad (3)$$

where  $k$  is the number of successes,  $n$  is the number of trials,  $p$  is the probability of success for each trial and  $\Gamma$  is the gamma function. The left fraction is the binomial coefficient and is more commonly written as  $\binom{n}{k}$  but the gamma function representation generalizes to non-integers.

In practice  $p$  may not be precisely known, but can be constrained by a prior distribution. To make averaging over the unknown value of  $p$  analytically tractable, we use a beta distribution  $B(p; \alpha_s, \beta_s)$  as a prior over  $p$ , where in this case  $\alpha_s$  corresponds to a prior weight towards higher  $p$ , and  $\beta_s$  to a prior weight towards lower  $p$ . Elicitation of a suitable prior from geologists with field experience suggests  $\alpha_s = 20, \beta_s = 1$ , resulting in a 95% credible lower limit of 85% on  $p$ . Integrating over the unknown value of  $p$  then leads to a beta-binomial likelihood:

$$P(k|n, \alpha, \beta) = \frac{\Gamma(n+1)}{\Gamma(k+1)\Gamma(n-k+1)} \int_0^1 p^k (1-p)^{n-k} \left[ \frac{p^\alpha (1-p)^\beta}{B(\alpha, \beta)} \right] dp \quad (4.1)$$

$$P(k|n, \alpha, \beta) = \frac{\Gamma(n+1)}{\Gamma(k+1)\Gamma(n-k+1)} \frac{\Gamma(k+\alpha)\Gamma(n-k+\beta)}{\Gamma(n+\alpha+\beta)} + \frac{\Gamma(\alpha)\Gamma(\beta)}{\Gamma(\alpha+\beta)} \quad (4.2)$$

(see Appendix A for full derivation of formula). This captures overdispersion resulting from unresolved sources of variation in the observation errors, such as distinct geologists interpreting rock formations differently (Gelman et al., 2013).

### 3.5. Markov chain Monte Carlo sampling

We use PT-MCMC to explore the parameter space, which is defined by our 3D geological model parameterization. PT-MCMC in Obsidian has

previously been evaluated by Scalzo et al. (2019), and yielded superior efficiency for similar levels of accuracy compared to other samplers. PT-MCMC operates by running a number of Markov chains in parallel, each sampling a modified version of the posterior:

$$P_i(\theta|D) \propto P(D|\theta)^{\beta^i} P(\theta) \quad (5)$$

where the inverse temperatures  $\{\beta_i\}$  form a decreasing sequence  $1 = \beta_0 > \beta_1 > \beta_2 > \dots > \beta_N > 0$ . Thus only the chain with  $\beta_0 = 1$  is sampling from the true posterior distribution, whereas the other chains explore versions of the problem with reduced influence from the data (a chain sampling in the limit  $\beta_i \rightarrow 0$  is sampling from the prior). Two chains are allowed to swap their most recent states  $\theta$  and  $\theta'$  with probability:

$$P_{\text{swap}} = \min\left(1, \left[\frac{P(D|\theta')}{P(D|\theta)}\right]^{\beta^* - \beta} \times \frac{P(\theta')}{P(\theta)}\right) \quad (6)$$

This method of sharing information among chains enables chain 0 to explore parts of parameter space visited by the other chains while still guaranteeing convergence to the true posterior distribution. At cessation of sampling only the samples from chain 0 are used.

Obsidian uses the adaptive version of the PT-MCMC algorithm described by Miaojejow et al. (2013), which continuously adapts both the scale of proposals within a chain and the temperature differences between chains in order to satisfy a target acceptance rate for swaps (we use 0.25; Atchad'e et al., 2011). The maximum allowed scale for adjustments is decreased to zero over time, ensuring that the adaptive algorithm will still produce samples from the desired posterior distribution. Obsidian's implementation is distributed, allowing a large number of cores to be used efficiently for sampling (McCalman et al., 2014; Beardmore et al., 2016).

The Metropolis-Hastings algorithm (Metropolis et al., 1953; Hastings, 1970) is used to sample parameters associated with each chain's target distribution. This algorithm makes a proposal  $\theta'$  chosen from a proposal distribution  $q(\theta'|\theta)$ , which is then accepted with probability

$$P_{\text{accept}} = \min\left(1, \frac{P(D|\theta')}{P(D|\theta)} \times \frac{P(\theta')}{P(\theta)} \times \frac{q(\theta|\theta')}{q(\theta'|\theta)}\right) \quad (7)$$

If the proposal is accepted, it is added to the chain; if it is rejected, a copy of the previous state is added to the chain. We use the preconditioned Crank–Nicolson MCMC proposal (Cotter et al., 2013; Hu et al., 2017; Rudolf and Sprung, 2018):

$$\theta' = \sqrt{(1 - \eta^2)} \theta_n + \eta u \quad (8)$$

where  $\theta_n$  is the state of the chain at iteration  $n$ ,  $\eta \in (0,1)$  is a step-size parameter, and  $u \sim P(\theta)$  is a random vector drawn from the (multivariate Gaussian) prior. When  $\eta \ll 1$ , the proposal reduces to a random walk, while for  $\eta \sim 1$  the proposal approaches a draw from the prior. This proposal was originally developed for use in inversions on function spaces, but it may also accelerate convergence as a within-chain proposal in high-dimensional parallel tempering problems (see Scalzo et al., 2019).

### 3.6. Experiment design

Two experiments were run, one incorporating the geological field observations and one without them. For both experiments, we run the Obsidian PT-MCMC with six parallel tempering temperature ladders (stacks), where each stack consists of twelve PT-MCMC chains. The likelihood of each chain is raised to the power of a different temperature in the ladder and the lowest temperature chain is the unnormalized likelihood. Samples are only collected for the lowest temperature chain. This setup has enough chains in each ladder to ensure geometric spacing between temperatures on the ladder, confirmed by empirical examination of the ladder, and has enough stacks to ensure sufficient confidence

in the convergence diagnostics, specifically the potential scale reduction factor diagnostic (see section 4.1). Both experiments were run on the same area of  $13.5 \text{ km} \times 13.5 \text{ km}$  for 96 h to ensure convergence for all rock property and control point parameters. Diagnostics for the experiment with field observations is presented below. Diagnostics for the experiment without field observations may be found in Supplementary Table A and not discussed in the text.

## 4. Results

### 4.1. Convergence diagnostics

Convergence diagnostics aid in evaluating whether the MCMC sampling has converged (i.e., whether sampling is occurring from the target distribution; Gelman et al., 2013). Convergence of the control point parameters occurred after only 12 h but the rock property parameters required approximately half of the total 96-h run time to reach convergence. Several techniques are listed here to confirm that our model outputs are statistically-valid, including (i) trace plots of the MCMC samples (Fig. 6a and b, Table 1), (ii) autocorrelation times and effective sample size (Fig. 6c, Table 1), (iii) potential scale reduction factor (Table 1), and (iv) Geweke score (Geweke, 1992) (Fig. 7).

Trace plots for modelled density and magnetic susceptibility show that: (a) chains initialized at different initial states have similar posterior densities, and (b) chains mix well, i.e., they sufficiently explore the support of the posterior distributions as determined by the parameters' respective priors (first column in each panel of Fig. 6). The Halfway Gneiss and Durlacher Supersuite have modelled densities of  $2.72 \pm 0.12$  and  $2.67 \pm 0.12 \text{ g cm}^{-3}$  (uncertainties quoted at two standard deviations [ $2\sigma$ ] here and throughout), respectively, and average modelled  $\log_{10}$  magnetic susceptibilities of  $-3.65 \pm 0.57$  and  $-2.60 \pm 0.07$  ( $2\sigma$ ), respectively (second column in each panel of Fig. 6). Compared to the Halfway Gneiss, a lower magnetic mean susceptibility and larger variance in magnetic susceptibility for the Durlacher Supersuite agrees with the prior density and magnetic measurements for both formations (Fig. 4). The lack of difference between the modelled densities of the Halfway Gneiss and Durlacher Supersuite (at  $2\sigma$ ) are also in agreement with the priors (Fig. 4).

The integrated autocorrelation time (IACT) is an estimate of the number of successive MCMC samples between statistically independent samples from the posterior distribution. It is given by:

$$\tau = \text{sum}\{-\infty, \infty\}P(\tau) \quad (9)$$

where  $P(\tau)$  is the normalized discrete autocorrelation function of the parameter values treated as a time series; a white noise time series, in which every sample is statistically independent of all the others, will have  $\tau = 1$ . Since any MCMC algorithm works by making proposals that adjust a chain's current location, the posterior samples they generate will necessarily be correlated in time (measured by sample index); this inefficiency is balanced by the ability of MCMC to preferentially sample regions of the parameter space with high posterior probability. Lower values of the IACT are desirable, since the statistical power of a MCMC chain of given finite length will vary inversely with the IACT. In practice, complex, high-dimensional posterior distributions can result in IACTs in the hundreds of thousands of samples (Ruggeri et al., 2015).

There are approximately 1.5 million total samples for each chain. However, samples from MCMC are correlated (third column in each panel of Fig. 6), which reduces the number of independent samples (i.e., the effective sample size) from the posterior distribution (Gelman et al., 2013). The MCMC autocorrelation is on the order of 1 in 12,000 to 1 in 14,000 independent samples per MCMC proposal for rock property parameters and 1 in 1000 to 1 in 15,000 independent samples for control point parameters (Table 1). This means that there are approximately 105–129 and 100–1000 independent samples for the rock property and control point parameters, respectively.

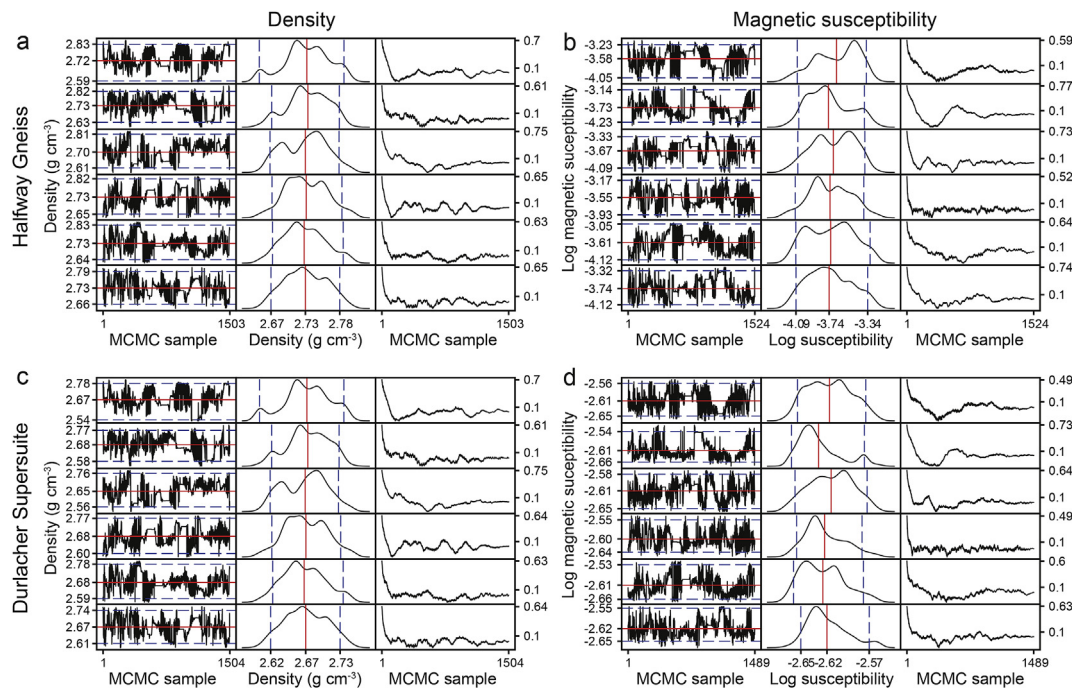


**Fig. 6.** MCMC diagnostics for the modelled Halfway Gneiss (a,b) and Durlacher Supersuite (c,d), for density (a,c) and magnetic susceptibility (b,d). Column 1 in each panel shows six of the twelve lowest temperature chains. Column 2 in each panel shows the distribution of petrophysical properties per chain. The red line and blue lines in columns 1 and 2 are the mean and  $2\sigma$ , respectively. Column 3 shows the autocorrelation time from the beginning of each chain to the end. Columns 1 and 3 MCMC iterations are thinned by 1000 (i.e., total number of samples is approximately 1.5 million per chain).

**Table 1**

Rock property diagnostics for density and magnetic susceptibility for both the Halfway Gneiss and Durlacher Supersuite.

Formation, petrophysical property	Mean	$-2\sigma$	$+2\sigma$	Autocorrelation time (k samples)	Effective $n$	$\hat{R}$
Halfway Gneiss, Rock Density (mGal)	2.72	0.13	0.11	11.61	129.1967	1.02
Halfway Gneiss, Log Susceptibility	-3.65	0.53	0.57	14.26	105.2075	1.03
Durlacher Supersuite, Rock Density (mGal)	2.67	0.13	0.11	11.59	129.4099	1.02
Durlacher Supersuite, Log Susceptibility	-2.61	0.05	0.09	13.32	112.6397	1.02

The potential scale reduction factor (PSRF), also known as the Gelman-Rubin statistic or  $\hat{R}$  (Gelman and Rubin, 1992), assesses convergence by comparing the variance between means of multiple chains relative to the average of the variance within chains to show how much an estimator of the marginal posterior variance will decrease as the number of samples increases (Cowles and Carlin, 1996; Brooks and Gelman, 1998). Suppose we have  $m$  chains with  $n$  samples each of a given scalar parameter (i.e. projection of the parameter set onto one of the variables of interest), and let  $\mu_i$  and  $\sigma_i^2$  denote the mean and variance of samples from each chain with  $1 \leq i \leq m$ . The PSRF is then given by

$$\hat{R} = \left( n \frac{1}{n} \right) + \left( \frac{1}{n} + \frac{1}{mn} \right) \frac{B}{W}, \quad (10)$$

where  $B/n = \text{var}(\mu_i)$  is the sample variance of the  $m$  within-chain means, and  $W = \langle \sigma_i^2 \rangle$  is the sample mean of the  $m$  within-chain variances. If the diagnostic is close to 1 then limited reductions in variance can be made from further sampling and the sampling has likely converged to the target distribution. All of our rock property and control point parameters have  $\hat{R} = 1.02 - 1.03$  and  $\hat{R} = 1.00 - 1.06$ , respectively (Table 1), which indicate convergence on the basis that the Gelman-Rubin statistic is less than the threshold of 1.10 (Gelman et al., 2013).

The convergence of the target distribution may also be evaluated using the Geweke score (Geweke, 1992), which is a z-score diagnostic that compares the mean of subsets of samples from the start and end of the MCMC chains. Using the samples from a single parameter sampled by

a single chain, we calculate

$$z = \sqrt{(\mu_{\text{initial}} - \mu_{\text{final}}) / (\sigma_{\text{initial}}^2 + \sigma_{\text{final}}^2)} \quad (11)$$

where the initial  $n_{\text{initial}}$  samples from the chain have mean  $\mu_{\text{initial}}$  and variance  $\sigma_{\text{initial}}^2$ , and the final  $n_{\text{final}}$  samples from the chain have mean  $\mu_{\text{final}}$  and variance  $\sigma_{\text{final}}^2$ . We use  $n_{\text{initial}} = n_{\text{final}} = 0.1n$  where  $n$  is the total chain length. A heuristic for convergence are Geweke scores between -2 and +2, indicating normality of the difference in means (Cowles and Carlin, 1996). We see convergence of our chains in terms of this diagnostic with Geweke scores of -1 to +1 and -0.5 to 1.5 for the density and magnetic susceptibility parameters, respectively, except for two chains (chain 2, density for both formations) which show large deviations (Fig. 7).

#### 4.2. Residuals from forward models

Aeromagnetic and gravity models from forward models are broadly comparable to their measured counterparts (Fig. 8a, d).

Aeromagnetic models effectively identify the NW-SE strike of magnetic lineaments in the northern half of the modelled volume (Fig. 8) that would be predicted from geological maps (Fig. 2). The NE-trending elongate unit in the southern half of the map, corresponding to the Durlacher Supersuite (Fig. 2), also shows limited discrepancies between modelled and measured data (Fig. 8). Aeromagnetic residuals display an approximately Gaussian distribution with a mean of 0 nT (i.e., equivalent

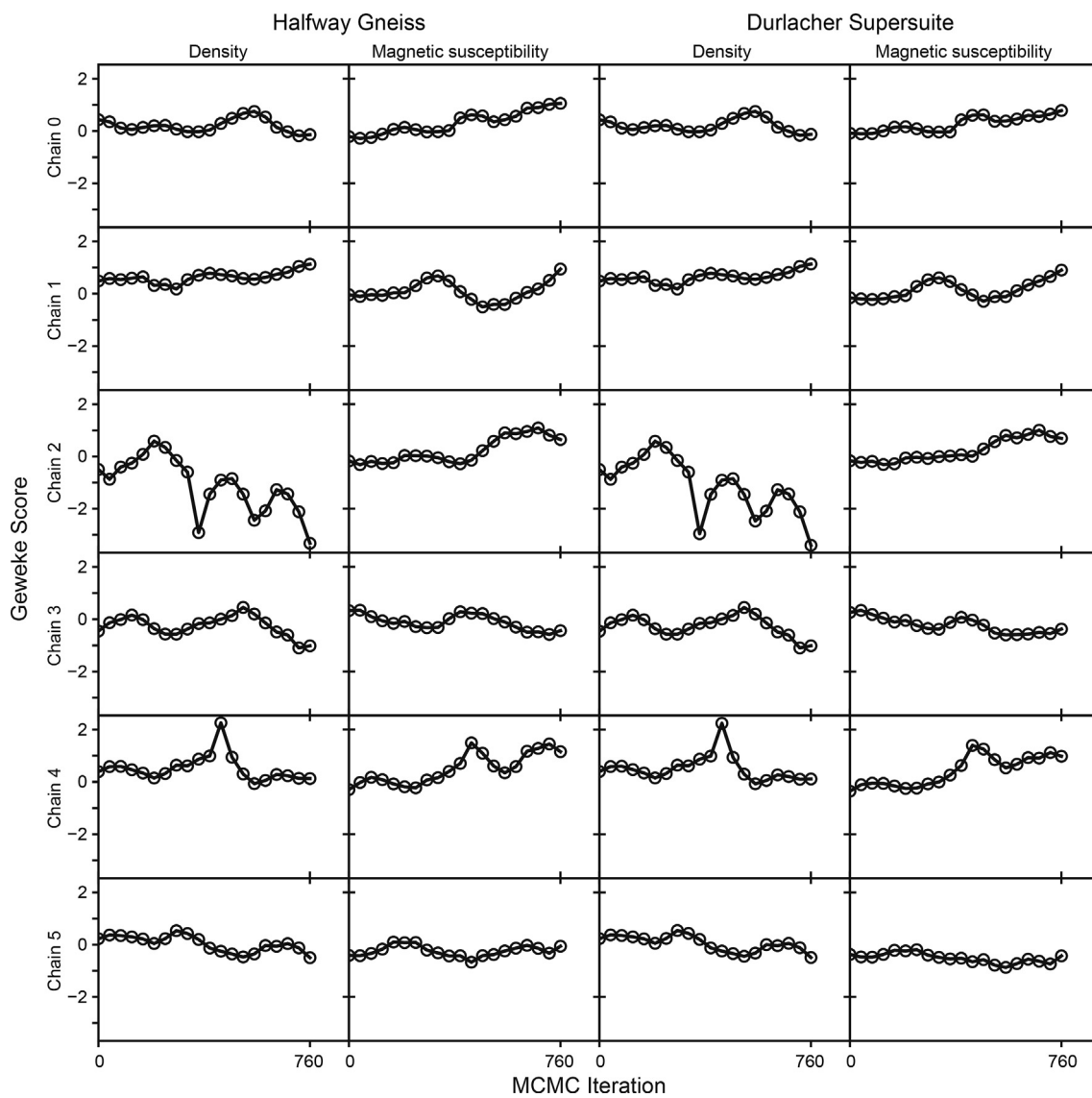


**Fig. 7.** Geweke scores for modelled densities and magnetic susceptibilities for the Halfway Gneiss and Durlacher Supersuite, shown for six chains.

to measured aeromagnetic data) and a range of  $+3.96 - 2.36$  nT ( $2\sigma$ ), which covers approximately 21% of the total magnetic range (Fig. 8). The  $\sim 21\%$  residual standard deviation is comparable to the standard deviation range of magnetic susceptibility values (Fig. 4). One region in the northwestern portion of the map has significantly higher magnetic field strength than modelled (Fig. 8).

Modelled gravity data effectively identifies the long-wavelength, N–S trending structure in the measured data but there are significant positive residuals in the south-west corner and negative residuals in the central-eastern portion of the modelled area (Figs. 2 and 8). Gravity residuals are positively skewed with a mean residual of 0 and a standard deviation of  $+3.96 - 2.36$  mGal ( $2\sigma$ , 20% of the total gravity range; Fig. 8). The gravity residual range of  $\sim 20\%$  is comparable to the standard deviation of density data (Fig. 4).

The forward modelled field observations have a posterior probability of success of approximately 80% (Fig. 9a–c). Five of 141 actual Halfway Gneiss observations have been misclassified as belonging to the Durlacher Supersuite, while most of the actual Durlacher Supersuite observations in its southeast corner have been misclassified as belonging to Halfway Gneiss (Fig. 9d–f). All the misclassifications occur within 1 km

of boundaries between geological units (Fig. 9e).

#### 4.3. Probability density of layer locations

Voxelized posterior distributions of the modelled volume reveal a strong probability contrast between regions of high certainty (defined as  $>95\%$ ) at the surface (Fig. 10). The modelled volume shows that the Durlacher Supersuite occupies the northeastern section of the region and an ellipsoidal inlier towards the southern extent of the  $13.5 \text{ km} \times 13.5 \text{ km}$  map (Fig. 10b). The remainder of the map shows Halfway Gneiss. Approximately along the Chalba Shear Zone (Fig. 10a), For the given model and data,  $\sim 300$ – $1000$  m widths of  $<95\%$  certainty separate regions of  $>95\%$  certainty (Fig. 10b). The uncertainty on the boundary between the ellipsoidal Durlacher Supersuite inlier and the Halfway Gneiss is constrained differently in different parts of the model. The horizontal distance for the boundary between the Durlacher Supersuite and Halfway Gneiss ( $<95\%$ ) is relatively tightly constrained along the NW and SW margins ( $\sim 450$  m), moderately constrained along the SE margin ( $\sim 750$ – $1100$  m) and poorly constrained towards the east (up to 2350 m; Fig. 10).

At depth, sub-vertical unit boundaries are maintained as informed by the prior (Figs. 1 and 2; seismic interpretation of Johnson et al. (2013)).

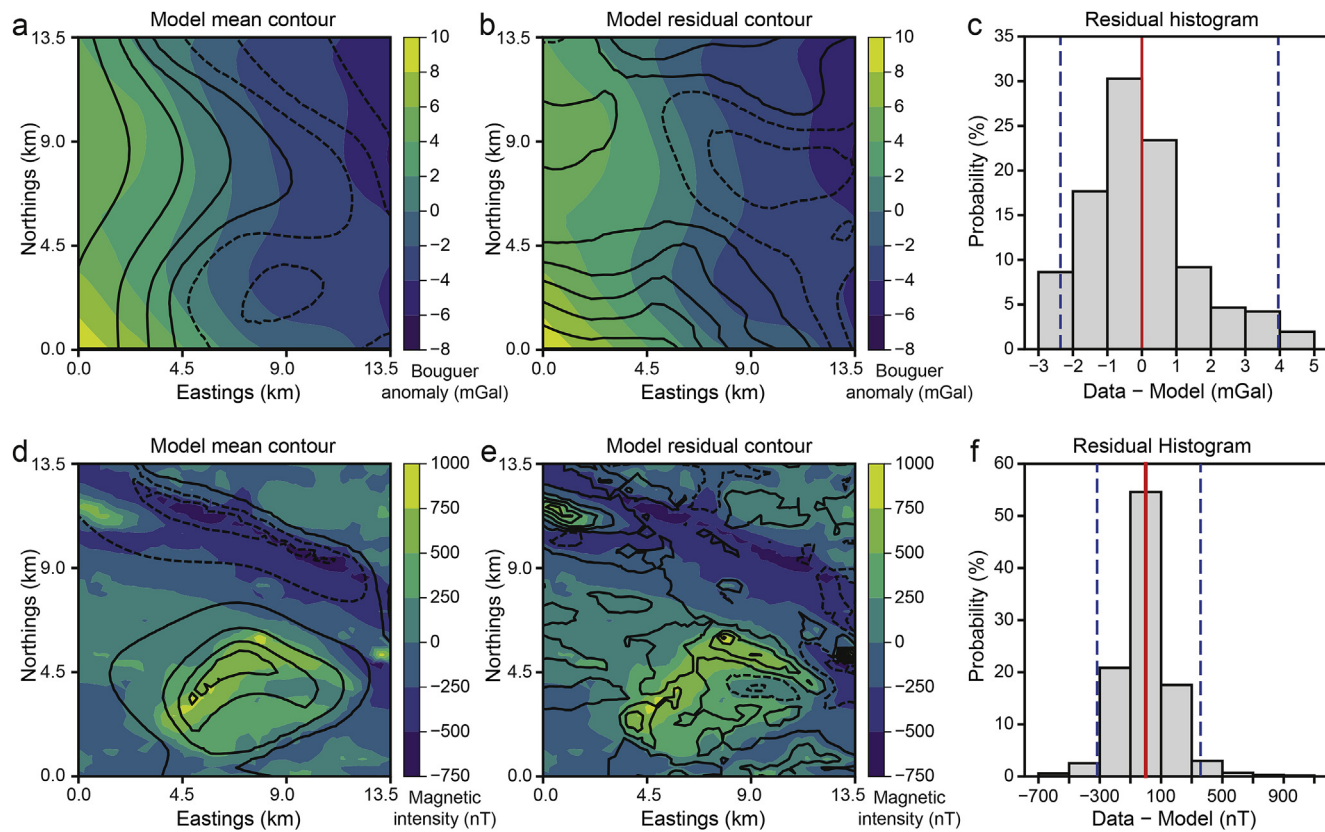


**Fig. 8.** Modelled Bouguer anomaly and magnetic intensity. Modelled mean contours of (a) Bouguer anomaly and (d) magnetic intensity compared to interpolated mean colored data. Modelled residual (i.e., data – model) contours for (b) Bouguer anomaly and (e) magnetic intensity compared to interpolated mean colored data. In (a–d), contour lines are in 2 mGal and 250 nT increments for gravity and magnetic intensity, respectively, where solid lines  $\geq 0$  and dashed lines  $< 0$ . Histograms of residuals for (c) Bouguer anomaly and (f) magnetic intensity.

The modelled cross-section yields dips of  $85^\circ$  near the surface, and progressively reducing in inclination to  $\sim 72^\circ$  at 4 km depth. In the cross-section, the horizontal distance between regions of  $>95\%$  certainty between the Halfway Gneiss or Durlacher Supersuite becomes progressively more diffuse, from  $\sim 420$  m to 1060 m between the surface and 4 km depth, respectively (Fig. 11). This translates to a percentage decrease in horizontal confidence of  $\sim 250\%$ . In other parts of the 3D model, regions of  $<95\%$  certainty can be as wide as  $\sim 2500$  m at depth (Fig. 11b).

## 5. Discussion

### 5.1. Validity of 3D models and comparison to geological maps and cross-sections

The fusion of geological field observations with gravity and magnetic data are valid on a statistical basis, including showing: (i) modelled petrophysical properties comparable with the prior (Figs. 4 and 6), (ii) adequate yield of independent samples (Fig. 6), (iii) sufficient exploration of the parameter space ( $\hat{R} < 1.1$ , Table 1), and (iv) convergence as indicated by Geweke scores primarily between  $-1$  and  $+1$  (Fig. 7). Aeromagnetic, gravity and field observations show mean residuals of  $\sim 0$  with  $2\sigma$  tails that are a maximum of  $\sim 20\%$  of the total dataset range (Fig. 8c,f). Aeromagnetic residuals are spatially uncorrelated except for a small region in the NW corner of the  $13.5 \text{ km} \times 13.5 \text{ km}$  area (Fig. 8b), indicating that the model captures relevant variation on the length scales of interest. Gravity residuals are systematically positive in the south, west and north, and negative in the east (Fig. 8e). This is primarily a function of a long-wavelength gravity response that is probably attained from the deep subsurface (Johnson et al., 2013), whereas the model aims to capture the shallow subsurface model ( $< 5$  km). Field observation

misclassifications are only found within 1 km of geological boundaries. The discrepancies between field observations and modelled geological units may be have resulted from the presence of other geological units (particularly those that are highly magnetic) that are then incorrectly modelled. Alternatively, some of the geological field observations may be in error; the eastern margin of the Durlacher Supersuite ‘inlier’ would be particularly interesting to re-investigate in the field (Fig. 10a). Additionally, more petrophysical data for the Halfway Gneiss and Durlacher Supersuite inside the modelled area may have yielded better priors for the geophysical surveys, which in turn would have corroborated better with the position of geological field observations. Ultimately, the data residuals are sufficiently small to have yielded a reliable model output despite some discrepancies.

The experiment that was run without field observations converged relatively successfully as well, although some dimensions had  $\hat{R}$  values as large as 1.3, above the threshold of 1.1 (Supplementary Table A). Qualitatively, the output looks broadly similar to the model without field observations (compare Fig. 10c and d). However, there is an over-assignment of the Durlacher Supersuite, particularly in the bottom right hand corner of the map. Thus, the experiment that incorporated field observations yielded better results, validating the use of field observations to yield more plausible geological models.

The voxelized posterior distributions of the modelled volume are visually comparable to geological maps and interpreted cross-sections made by GSWA (Johnson et al., 2012; Figs. 2 and 10). At the surface, the NW–SE striking Chalba Shear Zone boundary between the Halfway Gneiss and Durlacher Supersuite and the ellipsoidal inlier of Durlacher Supersuite are effectively captured in the models, with  $<1$  km of  $<95\%$  confidence regions separating  $>95\%$  certainty domains (Fig. 10). A thin sliver of mapped Durlacher Supersuite that encroaches the map in the

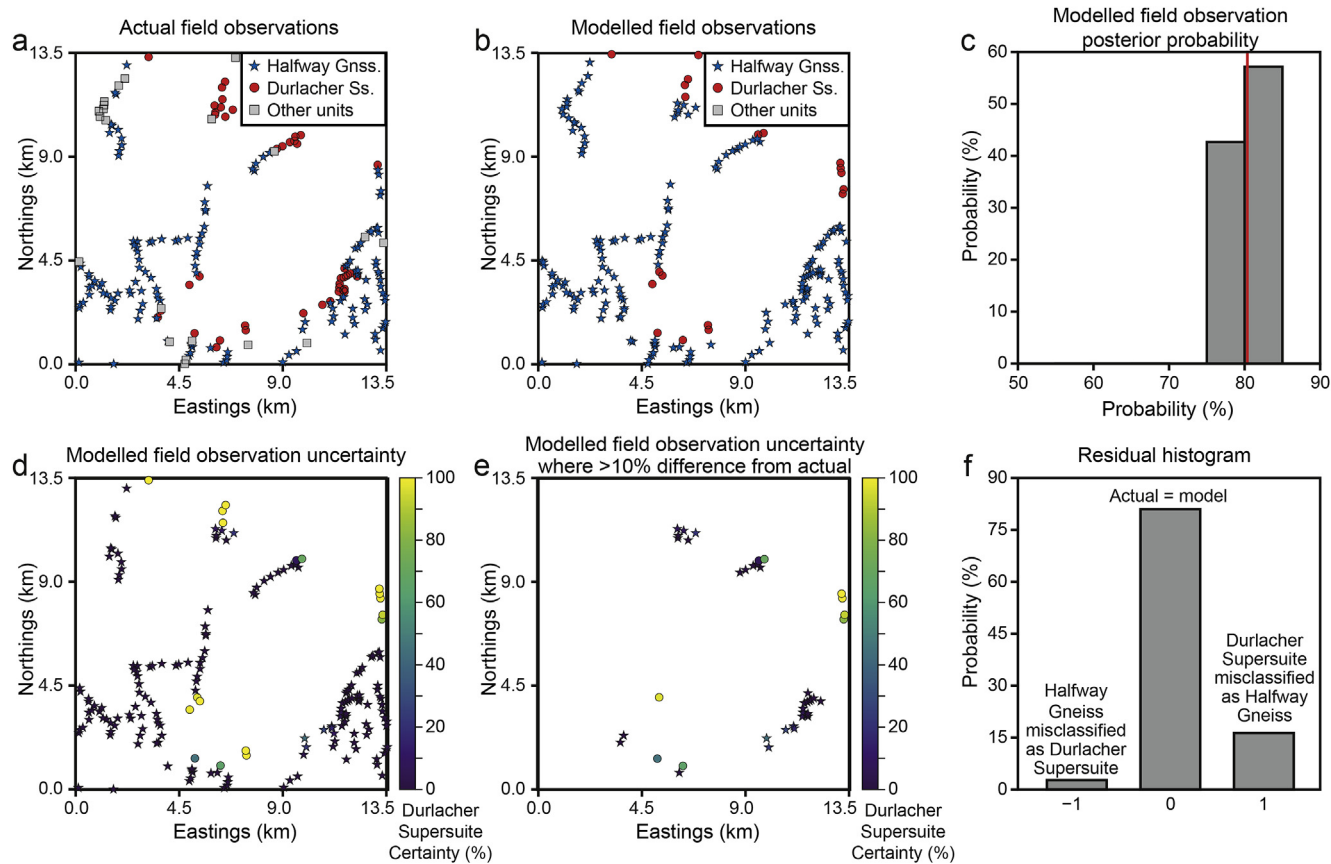


**Fig. 9.** Actual vs. modelled field observations. (a) Actual field observations. (b) Modelled field observations, showing highest probability geological unit. (c) Modelled field observation posterior probability. (d) Modelled field observations with uncertainty. (e) Modelled field observations with uncertainty, where >10% different from actual field observations. (f) Residual histogram, where  $-1$  is Durlacher Supersuite misclassified as Halfway Gneiss,  $0$  is correctly classified and  $1$  is Halfway Gneiss misclassified as Durlacher Supersuite.

NW section of the map (at  $\sim 7255500$  mN) is modelled as Halfway Gneiss (Fig. 10), which explains why an abnormally high magnetic residual is present there (Fig. 8). This discrepancy is probably a result of the aeromagnetic data integrating the magnetic response of Halfway Gneiss at depth.

In three-dimensions, the model maintains the sub-vertical to steeply-dipping regions of  $<95\%$  certainty (i.e., geological boundaries; Fig. 11). This is particularly well viewed in the X-Y cross-section, where the posterior distributions reveal sub-vertical dips ( $>85^\circ$ ) that are comparable to the sub-vertical dips measured in the field and propagated into interpreted cross-sections (Figs. 2 and 10). The modelled inclinations at 4 km depth are shallower ( $72^\circ$ ) than those interpreted by GSWA, which maintain dips of  $>85^\circ$  at 4 km (Fig. 2). Seismic interpretation data indicates that the Chalba Shear Zone is dipping at  $\sim 65^\circ$  at 4 km depth (Fig. 2), more comparable to our modelled dips than those interpreted from geological mapping. However, with the lack of drill hole data, it is difficult to know exactly whether the dips obtained from seismic interpretations, geological cross-section interpretation or modelled posterior distributions are correct. Despite these small discrepancies, the broad architecture of the model maintains the framework inferred from geological maps and cross-sections.

Another important output is that the modelled posterior distributions reveal that the Durlacher Supersuite is separated into two domains at the surface and shallow subsurface, one NE of the Chalba Shear Zone and the other as an ellipsoidal inlier, with a  $\sim 2.5$  km-wide region of  $>95\%$  confidence Halfway Gneiss separating the two regions (Fig. 10). This model output is corroborated at the surface by geological mapping across the region (Fig. 2). The fact that the Durlacher Supersuite is modelled into two domains demonstrates that its geophysical properties are

sufficiently different from the Halfway Gneiss to correctly identify the supersuite. It was uncertain whether this was possible given that the Durlacher Supersuite comprises multiple granitoid domains (Sheppard et al., 2005). An additional query was whether the spur of Halfway Gneiss between the two Durlacher Supersuite domains continued at depth or was truncated in the near subsurface. Our results suggest that the spur of Halfway Gneiss continues until at least 4 km as assumed from geological mapping. However, we do caution this finding because of the limitation of Obsidian to effectively incorporate deformed structures (see below).

## 5.2. Implications and limitations for quantification of uncertainty in 3D geological models

At the surface and near-surface (1 km), our model results are similar to independently-constrained geological maps and interpreted cross-sections (Figs. 2 and 10), which are useful for mineral exploration applications that rarely exceed economic deposit depths of 1 km (McFadden et al., 2012). This similarity is in spite that the prior distribution for the depth to the geological contact was Gaussian with standard deviations of 5 km at each control point (i.e., very permissive). Any further assumptions about depth to contact were uninformative by design to encapsulate the uncertainty in formulating initial models in areas about which little prior information is known (e.g., in greenfields mineral exploration). We emphasize that in well-studied areas our approach is unrealistic but for the purposes of mineral exploration in partially-covered terranes this approach is effective in broadly identifying geological boundaries. At the surface, distances between domains of  $>95\%$  confidence rarely exceed 1 km, although the eastern part of the ellipsoidal Durlacher Supersuite

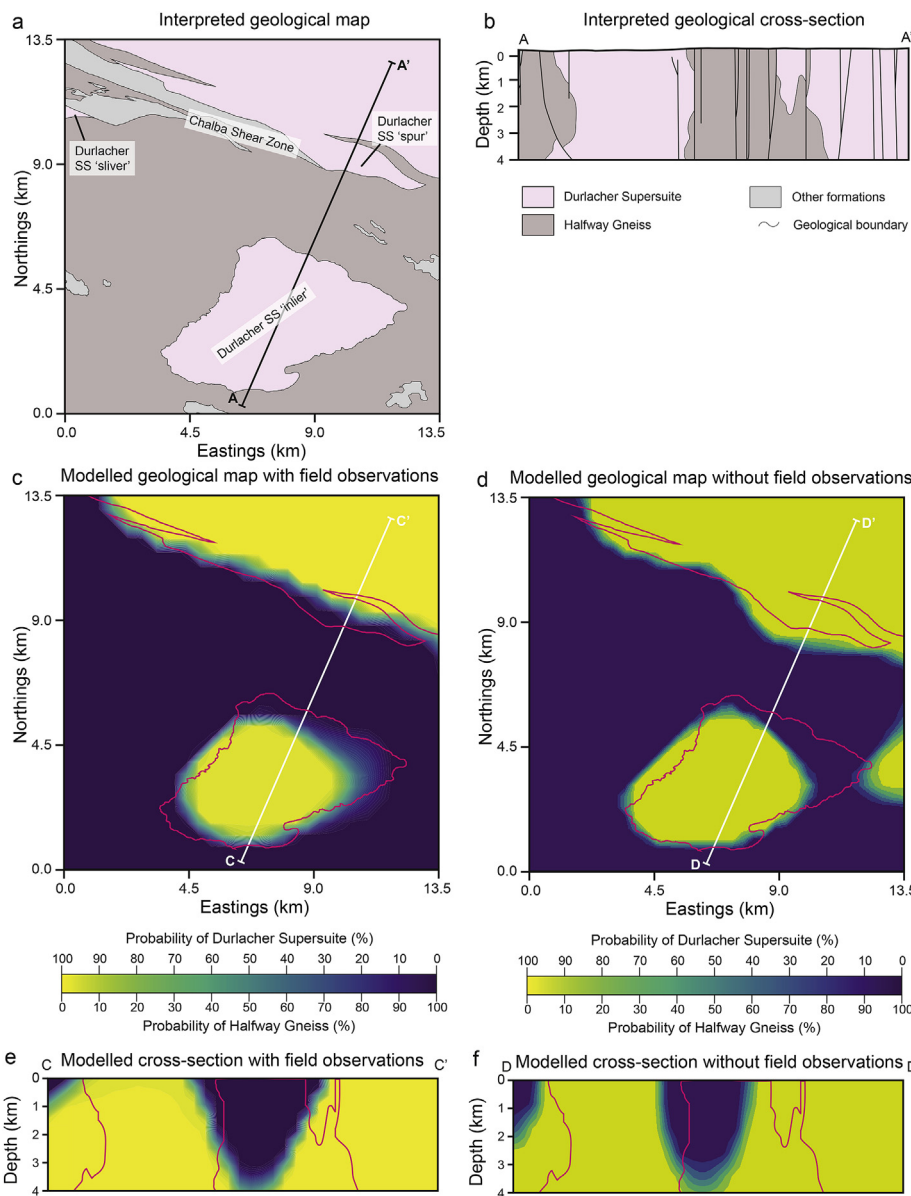


**Fig. 10.** Voxelized posterior distributions of 2D interfaces of the geological model compared to simplified GSWA maps and cross-sections. (a) Simplified geological map from Fig. 2, showing interpreted boundaries for the Durlacher Supersuite, Halfway Gneiss and other formations (undifferentiated), after Johnson et al. (2012). (b) Interpreted geological cross-section through A-A' in (a), after Johnson et al. (2012). (c) Model of the surface, with overlain pink line representing interpreted boundaries from (a). (d) Model of the surface when geological field observations are not used in the model, with overlain pink line representing interpreted boundaries from (a). (e) Modelled cross-section through C-C' in (c). (f) Modelled cross-section through D-D' in (d). All cross-sections have 1:1 horizontal to vertical aspect ratios.

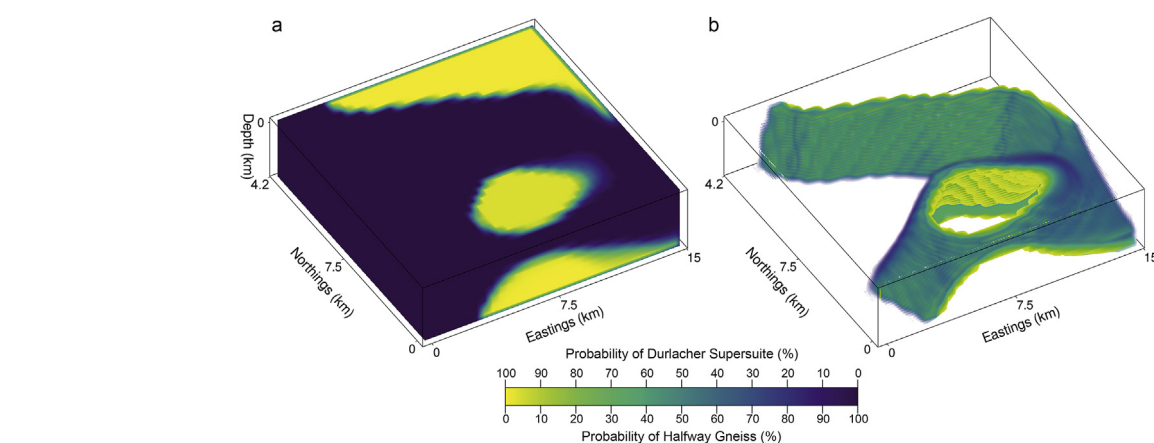


**Fig. 11.** Voxelized posterior distributions in 3D of the model with field observations, looking towards the northeast. (a) Probability of Halfway Gneiss and Durlacher Supersuite. (b) Same as (a) but only showing regions between 5 and 95% probability (i.e., the interface between the Durlacher Supersuite and Halfway Gneiss).

inlier are as wide as ~2350 m. The minimum horizontal distance of <95% uncertainty at geological boundaries appears is ~400 m, which appears to be inherently linked to the line spacing of the aeromagnetic survey. Given that the gravity survey and geological field observations are far more widely spaced, and therefore have less control on the model outputs, the aeromagnetic data distribution is probably the dominant control on the width of uncertain regions. For geological mapping applications (particularly in the mineral exploration sector), geological mapping in these uncertain regions (if outcrop is available) and/or high-resolution geophysical surveys across these small regions of uncertainty provide targeted and cost-effective methods of yielding better 3D geological models. Where such regions are under cover and drilling is required to establish formation contacts, our results could also aid in constraining which areas should be drilled first to maximize information gain.

For deep applications (e.g., depth to sedimentary basement or depth to Moho), our models require Bayesian incorporation of additional geophysical and geological data, such as active seismic (Johnson et al., 2013), passive seismic (Zhu and Kanamori, 2000) or deep drill hole geological observations (e.g., petroleum wells; McCalman et al., 2014; Beardsmore et al., 2016). The incorporation of structural measurement at the surface and in drill core (e.g., faults, folds) could also aid in informing the prior, particularly when seismic data are unavailable, to provide geologically-feasible models at the surface and shallow subsurface. Other geophysical surveys (e.g., magnetotellurics, radiometrics) could significantly improve the model certainty by identifying other variables in which geological units can have different rock properties.

The similarity of geophysical responses from different geological units in terranes that are broadly granitic (e.g., Halfway Gneiss and Durlacher Supersuite) has meant that the time to reach convergence is significantly greater than studies with units that display vastly different rock properties (McCalman et al., 2014; Beardsmore et al., 2016). The limiting factor is the ability to explore very high-dimensional posteriors that result from a large-scale non-parametric model (i.e. the number of control points at a given resolution scales exponentially with area). Our modelled area is 13.5 km × 13.5 km, which is useful for local-scale mineral exploration or detailed geological mapping, but may not be useful for reconnaissance-scale mineral exploration or terrane-scale geological modelling. Although our convergence times are not prohibitive for up-scaling the model to, for example 100 km × 100 km, computational time becomes difficult for developing 3D geological models for significantly larger areas (e.g., the entire Gascoyne Province). Incorporation of other data types (see above) may be part of the solution but these all rely on hand sample petrophysical measurements, which are not routinely collected, let alone reported in the geosciences. To solve the paucity of petrophysical data compared to geophysical surveys, the MCMC sampler could be modified to a reversible jump scheme (Green, 1995; Sambridge, 2013), which is able to define the number of layers, sampling over rock categories to define a baseline prior irrespective of available rock property data.

An important limitation relates to the confidence of geological field observations. This study has simplified the probability distribution of each field observation to a single beta-binomial distribution, when different supporting data (age, geochemistry, sample descriptions) will provide different likelihoods. Probability distributions of samples that have, for example, age and geochemical data, should be significantly more confident than samples that only have hand sample descriptions. However, the exact range of probabilities to ascribe to these samples still requires some user input. To make this process Bayesian and fully remove operator bias in assigning probabilities to field observations, an independent study will need to be conducted that purely assesses the likelihood of geological field observations, taking into account information like age data, geochemistry data and sample descriptions.

Another limitation of the current model is that only two geological units are modelled. In this study, the rationale for such a simplification is that the Halfway Gneiss and Durlacher Supersuite comprise >90% of the

surface geological units (Fig. 2) but this will rarely be the case in other problems. Integration of volumetrically-minor geological units may be vitally important with respect to mineral exploration or unravelling tectonic histories (e.g., Li-bearing pegmatites; Kesler et al., 2012). A major impediment to effectively modelling these volumetrically-minor units is the line spacing for different geophysical surveys and the potential paucity of geological field observations. In areas that are covered by shallow regolith or sedimentary cover, the problem of modelling volumetrically-minor units is exacerbated due to unavailability of geological surface measurements. Here, the only solution is to have drill hole geological information. Integration of drill hole geological units is already possible to build into the modelling process but moderately deep (>100 m) drill hole data are lacking for the modelled part of the Gascoyne Province. The Obsidian package – originally designed for sedimentary basins – inherently has limitations when applied to more complex geological geometries as are common in metamorphic terranes. Incorporation of Obsidian's advanced sampling methods with more sophisticated 3D modeling methods such as the implicit surface approach used by GemPy (de la Varga et al., 2019) can improve future geological modelling.

## 6. Conclusions

Bayesian integration of geological field observations with geophysical survey data yield statistically-reliable and geologically-plausible 3D models at the surface and shallow subsurface (< 4 km). For the given model and data, approximately 89% of the model area has > 95% certainty. Regions of < 95% certainty are found exclusively within 1 km of mapped or inferred geological boundaries. The widths and positions of regions with < 95% certainty are primarily a consequence of lack of geophysical, petrophysical or geological data. Our results indicate that these widths of these uncertain regions can be reduced by targeted geophysical surveys, petrophysical data collection and/or geological mapping. The integration of drill hole geological data and geophysical surveys with higher wavelengths (e.g., active seismic) are required to model deeper into the Earth's crust. Ultimately, the fusion of surface geological observations with geophysical data yield robust 3D geological models with narrow uncertainty regions at the surface and shallow subsurface that will be especially valuable for mineral exploration and the development of 3D geological models under cover. We anticipate that this framework provides a foundation for future applications in igneous and metamorphic terranes, particularly in the mineral exploration sector and especially in exploration under cover (McFadden et al., 2012).

### 6.1. Code and data availability

Aeromagnetic survey (Geological Survey of Western Australia, 1996) and gravity (Mathews and Jecks, 2010) data and metadata are freely available from the Geophysical Archive Data Delivery System ([www.geoscience.gov.au/geophysical-data-delivery](http://www.geoscience.gov.au/geophysical-data-delivery)). Petrophysical data are from Aitken et al. (2014). Geological field observations are available from WAROX, a database managed by the Geological Survey of Western Australia (GSWA). Geological field observation data may be directly requested from GSWA.

Model code is stored on Zenodo (<https://doi.org/10.5281/zenodo.2580422>).

### Declaration of competing interest

The authors declare that they have no known competing financial interests or personal relationships that could have appeared to influence the work reported in this paper.

### Acknowledgements

This manuscript benefited significantly from detailed comments of

four anonymous reviewers, G. Laurent, E. de Kemp, S. Johnson and the editorial handling of J. Alcalde and C. J. Spencer. G.A. Houseman is thanked for discussions and comments on an early version of this manuscript. This research was funded by the Science and Industry Endowment Fund as part of The Distal Footprints of Giant Ore Systems: UNCOVER Australia Project (RP04-063) — Capricorn Distal Footprints.

## Appendix A. Supplementary data

Supplementary data to this article can be found online at <https://doi.org/10.1016/j.gsf.2020.04.015>.

## References

- Abedi, M., Norouzi, G.-H., 2012. Integration of various geophysical data with geological and geochemical data to determine additional drilling for copper exploration. *J. Appl. Geophys.* 83, 35–45.
- Agangi, A., Plavsa, D., Reddy, S.M., Olierook, H., Kylander-Clark, A., 2020. Compositional modification and trace element decoupling in rutile: insight from the Capricorn Orogen, Western Australia. *Precambrian Res.* 345, 105772.
- Aitken, A.R.A., Joly, A., Dentith, M.C., Johnson, S.P., Thorne, A.M., Tyler, I.M., 2014. 3D Architecture, Structural Evolution, and Mineral Prospectivity of the Gascoyne Province. Report 123. Geological Survey of Western Australia, Perth, Australia.
- Atchad'e, Y., Fort, G., Moulines, E., Priouret, P., 2011. Adaptive Markov Chain Monte Carlo: Theory and Methods. In: Barber, D., Cemgil, A.T., Chiappa, S. (Eds.), *Bayesian Time Series Models*. Cambridge University Press.
- Beardsmore, G., Durrant-Whyte, H., McCalman, L., O'Callaghan, S., Reid, A., 2016. A Bayesian inference tool for geophysical joint inversions. *ASEG Extebd. Abstr.* 2016, 1–10.
- Bijani, R., Lelièvre, P.G., Ponte-Neto, C.F., Farquharson, C.G., 2017. Physical-property-, lithology-and-surface-geometry-based joint inversion using Pareto Multi-Objective Global Optimization. *Geophys. J. Int.* 209, 730–748.
- Bosch, M., Meza, R., Jiménez, R., Höning, A., 2006. Joint gravity and magnetic inversion in 3D using Monte Carlo methods. *Geophysics* 71, G153–G156.
- Brooks, S., Gelman, A., Jones, G., Meng, X.-L., 2011. *Handbook of Markov Chain Monte Carlo*. CRC Press.
- Brooks, S.P., Gelman, A., 1998. General methods for monitoring convergence of iterative simulations. *J. Comput. Graph. Stat.* 7, 434–455.
- Cawood, P.A., Korsch, R.J., 2008. Assembling Australia: Proterozoic building of a continent. *Precambrian Res.* 166, 1–35.
- Chandra, R., Müller, R.D., Azam, D., Deo, R., Butterworth, N., Salles, T., Cripps, S., 2019. Multicore parallel tempering Bayeslands for basin and landscape evolution. *Geochem. Geophys. Geosyst.* 20, 5082–5104. <https://doi.org/10.1029/2019GC008465>.
- Cotter, S.L., Roberts, G.O., Stuart, A.M., White, D., 2013. MCMC methods for functions: modifying old algorithms to make them faster. *Stat. Sci.* 28, 424–446.
- Cowles, M.K., Carlin, B.P., 1996. Markov chain Monte Carlo convergence diagnostics: a comparative review. *J. Am. Stat. Assoc.* 91, 883–904.
- de la Varga, M., Schaaf, A., Wellmann, F., 2019. GemPy 1.0: open-source stochastic geological modeling and inversion. *Geosci. Model Dev.* 12, 1–32. <https://doi.org/10.5194/gmd-12-1-2019>.
- Dentith, M., Mudge, S.T., 2014. *Geophysics for the Mineral Exploration Geoscientist*. Cambridge University Press.
- Earl, D.J., Deem, M.W., 2005. Parallel tempering: theory, applications, and new perspectives. *Phys. Chem. Chem. Phys.* 7, 3910–3916.
- Fullagar, P.K., Pears, G.A., McMonies, B., 2008. Constrained inversion of geologic surfaces—pushing the boundaries. *Lead. Edge* 27, 98–105.
- Gelman, A., Rubin, D.B., 1992. Inference from iterative simulation using multiple sequences. *Stat. Sci.* 7, 457–472.
- Gelman, A., Stern, H.S., Carlin, J.B., Dunson, D.B., Vehtari, A., Rubin, D.B., 2013. *Bayesian Data Analysis*. Chapman and Hall/CRC.
- Geological Survey of Western Australia, 1996. Bangemall Basin, Job Number 2048. Perth, Western Australia.
- Geweke, J., 1992. Evaluating the Accuracy of Sampling-Based Approaches to the Calculation of Posterior Moments. *Bayesian Statistics*. University Press, Minneapolis, pp. 169–193.
- Geyer, W., 1993. The importance of suppression of turbulence by stratification on the estuarine turbidity maximum. *Estuar. Coast* 16, 113–125.
- Giraud, J., Lindsay, M., Ogarko, V., Jessell, M., Martin, R., Pakyuz-Charrier, E., 2019. Integration of geological uncertainty into geophysical inversion by means of local gradient regularization. *Solid Earth* 10, 193–210.
- Giraud, J., Pakyuz-Charrier, E., Jessell, M., Lindsay, M., Martin, R., Ogarko, V., 2017. Uncertainty reduction through geologically conditioned petrophysical constraints in joint inversion. *Geophysics* 82, ID19–ID34.
- Gradstein, F.M., Ogg, J.G., Schmitz, M.D., Ogg, G.M., 2012. *The Geologic Time Scale 2012* 2-Volume Set, vol. 2. Elsevier, Oxford, U.K.
- Green, P.J., 1995. Reversible jump Markov chain Monte Carlo computation and Bayesian model determination. *Biometrika* 82, 711–732.
- Grose, L., Laurent, G., Aillères, L., Armit, R., Jessell, M., Cousin-Dechenau, T., 2018. Inversion of structural geology data for fold geometry. *J. Geophys. Res.: Solid Earth* 123, 6318–6333.
- Guillen, A., Calcagno, P., Courrioux, G., Joly, A., Ledru, P., 2008. Geological modelling from field data and geological knowledge: Part II. Modelling validation using gravity and magnetic data inversion. *Phys. Earth Planet. In.* 171, 158–169.
- Hapke, C., Plant, N., 2010. Predicting coastal cliff erosion using a Bayesian probabilistic model. *Mar. Geol.* 278, 140–149.
- Hastings, W.K., 1970. Monte Carlo sampling methods using Markov Chains and their applications. *Biometrika* 57, 97–109.
- Hu, Z., Yao, Z., Li, J., 2017. On an adaptive preconditioned Crank–Nicolson MCMC algorithm for infinite dimensional Bayesian inference. *J. Comput. Phys.* 332, 492–503.
- Hukushima, K., Nemoto, K., 1996. Exchange Monte Carlo method and application to spin glass simulations. *J. Phys. Soc. Jpn.* 65, 1604–1608.
- Jessell, M., Aillères, L., De Kemp, E., Lindsay, M., Wellmann, J.F., Hillier, M., Laurent, G., Carmichael, T., Martin, R., 2014. Next Generation Three-Dimensional Geologic Modeling and Inversion, vol. 18. Society of Economic Geologists Special Publication, pp. 261–272.
- Jessell, M., Pakyuz-Charrier, E., Lindsay, M., Giraud, J., De Kemp, E., 2018. Assessing and Mitigating Uncertainty in Three-Dimensional Geologic Models in Contrasting Geologic Scenarios, vol. 21. Society of Economic Geologists Special Publication, pp. 63–74.
- Jessell, M.W., Aillères, L., de Kemp, E.A., 2010. Towards an integrated inversion of geoscientific data: what price of geology? *Tectonophysics* 490, 294–306.
- Johnson, S.P., Korhonen, F.J., Kirkland, C.L., Cliff, J.B., Belousova, E.A., Sheppard, S., 2017. An isotopic perspective on growth and differentiation of Proterozoic orogenic crust: from subduction magmatism to cratonization. *Lithos* 268–271, 76–86.
- Johnson, S.P., Sheppard, S., Groenewald, P.B., Farrell, T.R., 2012. Yinnetharra, WA sheet 2148. Geological Survey of Western Australia, 1:100 000 Geological Series.
- Johnson, S.P., Sheppard, S., Rasmussen, B., Wingate, M.T.D., Kirkland, C.L., Muhling, J.R., Fletcher, I.R., Belousova, E.A., 2011. Two collisions, two sutures: punctuated pre-1950 Ma assembly of the West Australian Craton during the Ophthalmian and Glenburgh Orogenies. *Precambrian Res.* 189 (3–4), 239–262.
- Johnson, S.P., Thorne, A.M., Tyler, I.M., Korsch, R.J., Kennett, B.L.N., Cutten, H.N., Goodwin, J., Blay, O., Blewett, R.S., Joly, A., Dentith, M.C., Aitken, A.R.A., Holzschuh, J., Salmon, M., Reading, A., Heinson, G., Boren, G., Ross, J., Costelloe, R.D., Fomin, T., 2013. Crustal architecture of the Capricorn orogen, western Australia and associated metallogeny. *Aust. J. Earth Sci.* 60, 681–705.
- Joly, A., Porwal, A., McCuaig, T.C., 2012. Exploration targeting for orogenic gold deposits in the Granites-Tanami Orogen: mineral system analysis, targeting model and prospectivity analysis. *Ore Geol. Rev.* 48, 349–383.
- Kass, R.E., Carlin, B.P., Gelman, A., Neal, R.M., 1998. Markov chain Monte Carlo in practice: a roundtable discussion. *Am. Statistician* 52, 93–100.
- Kesler, S.E., Gruber, P.W., Medina, P.A., Keoleian, G.A., Everson, M.P., Wallington, T.J., 2012. Global lithium resources: relative importance of pegmatite, brine and other deposits. *Ore Geol. Rev.* 48, 55–69.
- Korhonen, F.J., Johnson, S.P., Wingate, M.T.D., Kirkland, C.L., Fletcher, I.R., Dunkley, D.J., Roberts, M.P., Sheppard, S., Muhling, J.R., Rasmussen, B., 2017. Radiogenic heating and craton-margin plate stresses as drivers for intraplate orogeny. *J. Metamorph. Geol.* 35, 631–661.
- Krapež, B., Müller, S.G., Fletcher, I.R., Rasmussen, B., 2017. A tale of two basins? Stratigraphy and detrital zircon provenance of the Palaeoproterozoic Turee Creek and Horseshoe basins of Western Australia. *Precambrian Res.* 294, 67–90.
- Li, Y., Oldenburg, D.W., 1996. 3-D inversion of magnetic data. *Geophysics* 61, 394–408.
- Li, Y., Oldenburg, D.W., 1998. 3-D inversion of gravity data. *Geophysics* 63, 109–119.
- Lindsay, M.D., Jessell, M.W., Aillères, L., Perrotty, S., de Kemp, E., Betts, P.G., 2013. Géodiversité: exploration of 3D geological model space. *Tectonophysics* 594, 27–37.
- Martin, D.M., Morris, P.A., 2010. Tectonic setting and regional implications of ca 2.2 Ga mafic magmatism in the southern Hamersley Province, Western Australia. *Aust. J. Earth Sci.* 57, 911–931.
- Mathews, L.R., Jecks, M.J., 2010. *Gascoyne Gravity Survey*, Report Number R2010006. Atlas Geophysics, Morley, Western Australia, pp. 1–93.
- McCalman, L., O'Callaghan, S.T., Reid, A., Shen, D., Carter, S., Krieger, L., Beardsmore, G., Bonilla, E.V., Ramos, F.T., 2014. Distributed Bayesian Geophysical Inversions, Thirty-Ninth Workshop on Geothermal Reservoir Engineering, Stanford University, Stanford, California, pp. 1–11. February 24–26, 2014.
- McFadden, P., Barnicoat, A., Blewett, R.S., Collet, D., Collins, W., Dransfield, M., Fitzgerald, D., Haydon, R., Hough, R., Hronsky, J., McCuaig, C., McWilliams, M., Müller, R.D., Whiting, T., Woodgate, P., 2012. Searching the Deep Earth: a Vision for Exploration Geoscience in Australia, UNCOVER, Australian Exploration Geoscience Research, Australian Academy of Science, Canberra, Australia, p. 47.
- Merdith, A.S., Collins, A.S., Williams, S.E., Pisarevsky, S., Foden, J.D., Archibald, D.B., Blades, M.L., Alessio, B.L., Armistead, S., Plavsa, D., Clark, C., Müller, R.D., 2017. A full-plate global reconstruction of the Neoproterozoic. *Gondwana Res.* 50, 84–134.
- Metropolis, N., Rosenbluth, A.W., Rosenbluth, M.N., Teller, A.H., Teller, E., 1953. Equation of state calculations by fast computing machines. *J. Chem. Phys.* 21, 1087–1092.
- Miasojedow, B., Moulines, E., Viola, M., 2013. An adaptive parallel tempering algorithm. *J. Comput. Graph. Stat.* 22, 649–664.
- Mosegaard, K., Tarantola, A., 1995. Monte Carlo sampling of solutions to inverse problems. *J. Geophys. Res.: Solid Earth* 100, 12431–12447.
- Oladyshkin, S., Class, H., Nowak, W., 2013. Bayesian updating via bootstrap filtering combined with data-driven polynomial chaos expansions: methodology and application to history matching for carbon dioxide storage in geological formations. *Comput. Geosci.* 17, 671–687.
- Olierook, H.K.H., Agangi, A., Plavsa, D., Reddy, S.M., Clark, C., Yao, W.-H., Occhipinti, S.A., Kylander-Clark, A.R.C., 2019a. Neoproterozoic hydrothermal

- activity in the West Australian Craton related to Rodinia assembly or breakup? *Gondwana Res.* 68, 1–12.
- Olierook, H.K.H., Sheppard, S., Johnson, S.P., Occhipinti, S.A., Reddy, S.M., Clark, C., Fletcher, I.R., Rasmussen, B., Zi, J.-W., Pirajno, F., LaFlamme, C., Do, T., Ware, B., Blandthorn, E., Lindsay, M., Lu, Y.-J., Crossley, R.J., Erickson, T.M., 2018. Extensional episodes in the Paleoproterozoic Capricorn Orogen, Western Australia, revealed by petrogenesis and geochronology of mafic-ultramafic rocks. *Precambrian Res.* 306, 22–40.
- Olierook, H.K.H., Taylor, R.J.M., Erickson, T.M., Clark, C., Reddy, S.M., Kirkland, C.L., Jahn, I., Barham, M., 2019b. Unravelling complex geologic histories using U-Pb and trace element systematics of titanite. *Chem. Geol.* 504, 105–122.
- Pakyuz-Charrier, E., Giraud, J., Ogarko, V., Lindsay, M., Jessell, M., 2018a. Drillhole uncertainty propagation for three-dimensional geological modeling using Monte Carlo. *Tectonophysics* 747–748, 16–39.
- Pakyuz-Charrier, E., Lindsay, M., Ogarko, V., Giraud, J., Jessell, M., 2018b. Monte Carlo simulation for uncertainty estimation on structural data in implicit 3-D geological modeling, a guide for disturbance distribution selection and parameterization. *Solid Earth* 9, 385–402.
- Pall, J., Chandra, R., Azam, D., Salles, T., Webster, J.M., Scalzo, R., Cripps, S., 2020. Bayesreef: A Bayesian inference framework for modelling reef growth in response to environmental change and biological dynamics. *Environ. Model. Software* 125, 104610. <https://doi.org/10.1016/j.envsoft.2019.104610>.
- Parker, R.L., 1977. Understanding inverse theory. *Annu. Rev. Earth Planet Sci.* 5, 35–64.
- Piechocka, A.M., Gregory, C.J., Zi, J.-W., Sheppard, S., Wingate, M.T.D., Rasmussen, B., 2017. Monazite trumps zircon: applying SHRIMP U–Pb geochronology to systematically evaluate emplacement ages of leucocratic, low-temperature granites in a complex Precambrian orogen. *Contrib. Mineral. Petrol.* 172, 63.
- Piechocka, A.M., Sheppard, S., Fitzsimons, I.C.W., Johnson, S.P., Rasmussen, B., Jourdan, F., 2018. Neoproterozoic  $^{40}\text{Ar}/^{39}\text{Ar}$  mica ages mark the termination of a billion years of intraplate reworking in the Capricorn Orogen, Western Australia. *Precambrian Res.* 310, 391–406.
- Rafferty, A.E., Lewis, S.M., 1996. Implementing Mcmc. Markov Chain Monte Carlo in Practice, pp. 115–130.
- Ramos, F.T., Bonilla, E., McCalman, L., O'Callaghan, S., Reid, A., Uther, W.T.B., Cambridge, M., Rawling, T., 2012. Bayesian Data Fusion for Geothermal Exploration. In: Proceedings of Australian Geothermal Energy Conference (AGEA 2012), Record 2012/73. Geoscience Australia, Canberra, Australia.
- Rasmussen, B., 2005. Radiometric dating of sedimentary rocks: the application of diagenetic xenotime geochronology. *Earth Sci. Rev.* 68, 197–243.
- Refsgaard, J.C., Christensen, S., Sonnenborg, T.O., Seifert, D., Højberg, A.L., Troldborg, L., 2012. Review of strategies for handling geological uncertainty in groundwater flow and transport modeling. *Adv. Water Resour.* 36, 36–50.
- Reid, A., Simon Timothy, O.C., Bonilla, E.V., McCalman, L., Rawling, T., Ramos, F., 2013. Bayesian Joint Inversions for the Exploration of Earth Resources. In: Proceedings of the Twenty-Third International Joint Conference on Artificial Intelligence. Beijing, China, pp. 2877–2884.
- Rudolf, D., Sprungk, B., 2018. On a generalization of the preconditioned Crank–Nicolson Metropolis algorithm. *Found. Comput. Math.* 18, 309–343.
- Ruggeri, P., Irving, J., Holliger, K., 2015. Systematic evaluation of sequential geostatistical resampling within MCMC for posterior sampling of near-surface geophysical inverse problems. *Geophys. J. Int.* 202, 961–975.
- Sambridge, M., 1999. Geophysical inversion with a neighbourhood algorithm—II. Appraising the ensemble. *Geophys. J. Int.* 138, 727–746.
- Sambridge, M., 2013. A parallel tempering algorithm for probabilistic sampling and multimodal optimization. *Geophys. J. Int.* 196, 357–374.
- Sambridge, M., Mosegaard, K., 2002. Monte Carlo methods in geophysical inverse problems. *Rev. Geophys.* 40, 3–1.
- Scalzo, R., Kohn, D., Olierook, H., Houseman, G., Chandra, R., Girolami, M., Cripps, S., 2019. Efficiency and robustness in Monte Carlo sampling of 3-D geophysical inversions with Obsidian v0.1.2: setting up for success. *Geosci. Model Dev. (GMD)* 12, 2941–2960.
- Scholl, C., Neumann, J., Watts, M.D., Hallinan, S., Mule, S., 2016. Geologically constrained 2D and 3D airborne EM inversion through cross-gradient regularization and multi-grid efficiency. *ASEG Extebd. Abstr.* 2016, 1–6.
- Seifert, D., Sonnenborg, T.O., Refsgaard, J.C., Højberg, A.L., Troldborg, L., 2012. Assessment of hydrological model predictive ability given multiple conceptual geological models. *Water Resour. Res.* 48.
- Selley, R.C., Sonnenborg, S.A., 2014. Elements of Petroleum Geology. Academic Press.
- Sen, M.K., Stoffa, P.L., 1996. Bayesian inference, Gibbs' sampler and uncertainty estimation in geophysical inversion. *Geophys. Prospect.* 44, 313–350.
- Shen, W., Ritzwoller, M.H., Schulze-Pelkum, V., Lin, F.-C., 2013. Joint inversion of surface wave dispersion and receiver functions: a Bayesian Monte-Carlo approach. *Geophys. J. Int.* 192, 807–836.
- Sheppard, S., Bodorkos, S., Johnson, S.P., Wingate, M.T.D., Kirkland, C.L., 2010a. The Paleoproterozoic Capricorn Orogeny: intracontinental reworking not continent–continent collision. *Geol. Surv. West. Aust. Rep.* 108, 33p.
- Sheppard, S., Fletcher, I.R., Rasmussen, B., Zi, J.-W., Muhling, J.R., Occhipinti, S.A., Wingate, M.T.D., Johnson, S.P., 2016. A new Paleoproterozoic tectonic history of the eastern Capricorn Orogen, Western Australia, revealed by U–Pb zircon dating of micro-tuffs. *Precambrian Res.* 286, 1–19.
- Sheppard, S., Johnson, S.P., Wingate, M.T.D., Kirkland, C.L., Pirajno, F., 2010b. Explanatory Notes for the Gascoyne Province. Geological Survey of Western Australia, Perth, Western Australia.
- Sheppard, S., Occhipinti, S.A., Nelson, D.R., 2005. Intracontinental reworking in the Capricorn orogen, western Australia: the 1680–1620 Ma Mangaroon orogeny. *Aust. J. Earth Sci.* 52, 443–460.
- Sheppard, S., Rasmussen, B., Muhling, J.R., Farrell, T.R., Fletcher, I.R., 2007. Grenvillian-aged orogenesis in the Palaeoproterozoic Gascoyne complex, western Australia: 1030–950 Ma reworking of the Proterozoic Capricorn orogen. *J. Metamorph. Geol.* 25, 477–494.
- Tarantola, A., Valette, B., 1982. Generalized nonlinear inverse problems solved using the least squares criterion. *Rev. Geophys.* 20, 219–232.
- van Ravenzwaaij, D., Cassey, P., Brown, S.D., 2018. A simple introduction to Markov chain Monte–Carlo sampling. *Psychon. Bull. Rev.* 25, 143–154.
- Wellmann, J.F., de la Varga, M., Murdie, R.E., Gessner, K., Jessell, M., 2018. Uncertainty estimation for a geological model of the Sandstone greenstone belt, Western Australia – insights from integrated geological and geophysical inversion in a Bayesian inference framework. *Geol. Soc. Lond. Spec. Publ.* 453, 41–56.
- Wellmann, J.F., Regenauer-Lieb, K., 2012. Uncertainties have a meaning: information entropy as a quality measure for 3-D geological models. *Tectonophysics* 526–529, 207–216.
- Ye, M., Pohlmann, K.F., Chapman, J.B., Pohll, G.M., Reeves, D.M., 2010. A model-averaging method for assessing groundwater conceptual model uncertainty. *Ground Water* 48, 716–728.
- Zheglova, P., Lelièvre, P.G., Farquharson, C.G., 2018. Multiple level-set joint inversion of traveltime and gravity data with application to ore delineation: a synthetic study. *Geophysics* 83, R13–R30.
- Zhu, L., Kanamori, H., 2000. Moho depth variation in southern California from teleseismic receiver functions. *J. Geophys. Res.: Solid Earth* 105, 2969–2980.